POLITECNICO DI MILANO

Scuola di Ingegneria Industriale e dell'Informazione

Master of Science in Aeronautical Engineering

OPTIMIZATION OF TILTROTOR CONVERSION MANOEUVRE USING LINEAR PARAMETER-VARYING MODELS

Supervisor:

Prof. Giuseppe Quaranta

Master Thesis by:

Antonio Righetti

Student ID: 767894

Academic Year 2015-2016

To my family,
Ilaria,
and my friends
who always supported me.

I've missed more than 9000 shots in my career.
I've lost almost 300 games. 26 times, I've been
trusted to take the game winning shot and missed.
I've failed over and over and over again in my life.
And that is why I succeed.

Michael Jordan

Acknowledgements

I would like to express my sincere gratitude to my advisor Prof. Giuseppe Quaranta for his guidance on writing this thesis and especially for his inexhaustible patience and encouragement.

I would also like to express my thanks to Vincenzo Muscarello for his suggestions and support.

Abstract

The conversion manoeuvre is that flight phase in which a tiltrotor changes from a helicopter to an airplane configuration and vice-versa. This work aims to optimize the conversion manoeuvre of a generic tiltrotor on different objectives. Considering conversion manoeuvre data from the XV-15 and from the contemporary V-22 Osprey and AW-609 tiltrotors a *typical conversion manoeuvre* is defined. This manoeuvre is then optimized trying to improve safety, reduce rotor blades flapping, pilot control effort and the conversion required time.
The conversion modelling is based on a database of XV-15 Linear-Time-Invariant (LTI) models scheduled on airspeed and nacelles angle parameters. Following the Modified Optimal Control pilot Model (MOCM) guidelines a virtual pilot in the form of an LQI controller is designed for each XV-15 LTI model. To obtain pilot commands that are replicable by a real helicopter pilot the control lever displacement derivatives are considered as control inputs. This allow to restrain the speed with which pilot acts on commands by an adequate choice of LQI input weights. To verify that commands movements respect pilot limitations the command derivative histories and commands spectrum are checked after simulations.
Availing of the Linear Parameter-Varying (LPV) technique the XV-15 LTI models database is linearly interpolated in the scheduling parameters and a nonlinear like model is obtained. The LQI gain matrixes are also linearly interpolated in the same scheduling parameters. Finally, the closed-loop system *XV-15 LPV model − virtual pilot* allows the simulation and study of the conversion manoeuvre on the whole conversion corridor domain.

Contents

List of Figures

Chapter 1

Introduction

1.1 The tiltrotor aircraft

The tiltrotor aircraft combines the advantages of vertical take-off and landing capabilities, inherent to the helicopter, with the forward speed, range and service ceiling of a fixed wing turboprop airplane. The tiltrotor allows runway-independent operations, potentially relieving airport congestion, and also has high-speed, long-range, all-weather flight capabilities. These remarkable advantages have been the propelling ingredients in the difficult developing process of this revolutionary aircraft.
A modern tiltrotor has a layout similar to a turboprop aircraft but instead of classical airplane props it mounts large helicopter like rotors coupled with turboshat engines on the wing tips. Rotors can tilt from a helicopter to an airplane like configuration through a nacelles tilting system that permit to rotate the whole engine-rotor assembly.

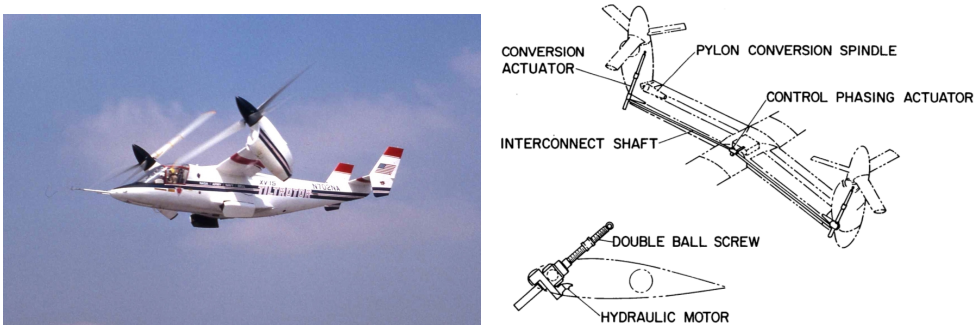

(a) XV-15 during conversion (b) XV-15 conversion system

Figure 1.1: Bell XV-15 tiltrotor

The tiltrotor can fly in three different modalities: it can take-off and hover like a helicopter with nacelles in vertical position, it can fly as an airplane when nacelles are completely rotate forward or it can fly in a hybrid configuration with nacelles partially rotated called conversion mode. The conversion manoeuvre regards that delicate phase in which rotors thrust changes it's orientation from vertical to horizontal bringing the aircraft to a forward flight in airplane configuration but also regards the opposite process in which the aircraft returns to a helicopter configuration. During the conversion from helicopter to airplane lift is increasingly generated by the wing, while rotors thrust becomes gradually horizontal. To land rotors are rotated up to guarantee the necessary ground-rotors clearance and a normal helicopter landing can be performed.

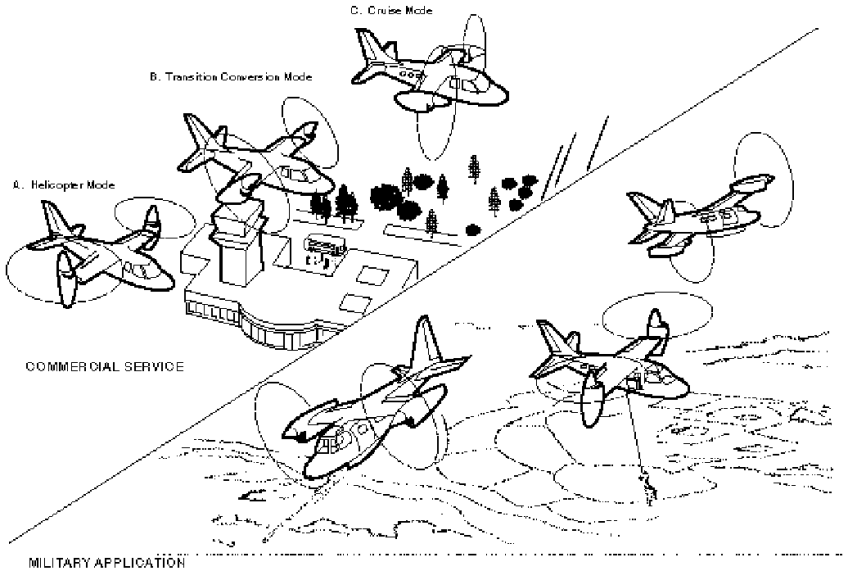

Figure 1.2: Tiltrotor conversion and missions examples

1.2 Tiltrotor history

The design work of Mario A. Guerrieri and Bob Lichten on what has been the first flying tiltrotor able to achieve a partial conversion started in 1945. They found the Transcendental Aircraft Company at New Castle, Delaware, in 1947. The Model 1-G was a small cantilever monoplane powered by a single 160 hp Lycoming O-290-A engine positioned in the fuselage that drove two three-blade rotors at wing tips. A series of contracts from the United States Air Force (USAF) financed the aircraft development until a Model 1-G suitable for flight testing was built. The tiltrotor made its first flight on July 6, 1954 while the first in-flight rotor-tilting took place

in December that year, and by April 1955, it was flying with 35° nacelles angle reaching speeds of 100 kn. On July 20, 1955, the aircraft suffered a control system failure causing it to crash into the Delaware River. A more powerful and aerodynamic refined tiltrotor was then built by Transcendental, the Model 2, that flew in 1956. However, US Government funds were then directed to the Bell XV-3 causing the Model 2 to be abandoned.

The Bell XV-3 was first flown on 11 August 1955. Until then a full conversion was never accomplished but the XV-3 successfully demonstrated the tiltrotor concept, accomplishing 110 transitions from helicopter to airplane mode between December 1958 and July 1962. The XV-3 program ended when the last prototype was severely damaged in a wind tunnel accident on 20 May 1966. The data and experience from the XV-3 program were key elements used to successfully develop the Bell XV-15.

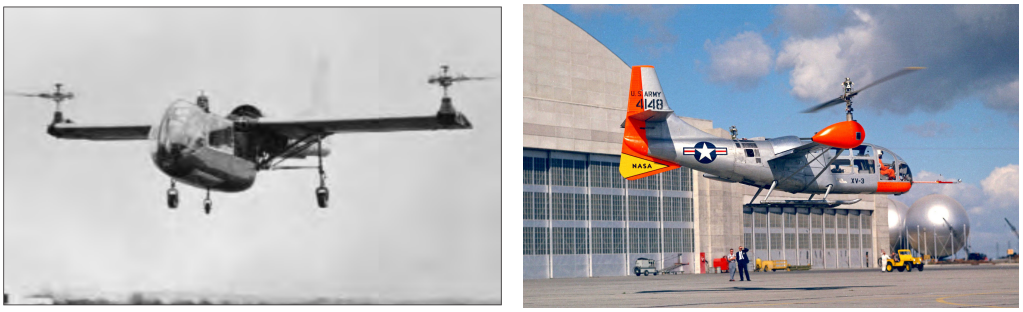

(a) Transcendental Model 1-G

(b) Bell XV-3

Figure 1.3: Historical tiltrotors

The Bell XV-15 experimental aircraft introduced a major design concept advance: instead of engines in the fuselage, the XV-15 moved the engines out to the rotating nacelles, directly coupled to the three blades rotors. There was still a driveshaft along the wings for emergency use to transfer power to the opposite rotor in case of engine failure, but that shaft did not normally carry any power loads, making it lighter. This new way to deliver power to rotors is still implemented in today tiltrotors. The XV-15 was used as bench test to support the V-22 Osprey military tiltrotor program and Bell/Agusta (later AgustaWestland) AW609 civilian medium tiltrotor transport aircraft.

The Bell Boeing V-22 Osprey first flew in 1989. The complexity and difficulties of being the first tiltrotor intended for military service in the world led to many years of development. The V-22 supplemented and then successfully replaced the

Boeing Vertol CH-46 Sea Knights. Since it's entering into service in June 2007 with the U.S. Marine Corps and Air Force, the Osprey has been deployed for troopship in several US military operations.

The AgustaWestland AW-609 is intended to be the first civilian tiltrotor. The AW609 drew on experience gained from Bell's earlier tiltrotors but there are much differences from predecessors. Among the many, it's the first tiltrotor with a pressurized cabin. It can accommodate nine passenger in the standard layout and for increased passenger comfort the cabin is also equipped with soundproofing. Along with the AW-609 certification process that should end in 2018 a new specific tiltrotor regulation is being made by certification agencies. This new norms will rule the future tiltrotors.

(a) Bell Boeing V-22 Osprey (b) AgustaWestland AW-609

Figure 1.4: Modern tiltrotors

1.2.1 Conversion corridor

The particular manoeuvre that distinguishes a tiltrotor is the conversion. A tiltrotor can safely execute this manoeuvre staying within a particular region of the aircraft airspeed - nacelles angle domain called "*conversion corridor*" because of it's particular shape. Every tiltrotor designed has its particular conversion corridor but they basically share the same form. Figure 1.5(a) qualitatively show the V-22 conversion corridor while figure 1.5(b) it's a detailed representation of the XV-15 conversion corridor.
The lower-left corridor boundary is the representation of the aircraft attitude and wing stall limits while the upper-right boundary represents rotors load limits. The more the tiltrotor stays away from these two boundaries during the conversion the safer is the manoeuvre. This imply that the safest manoeuvre is that one that keeps the aircraft at the center of the conversion corridor.

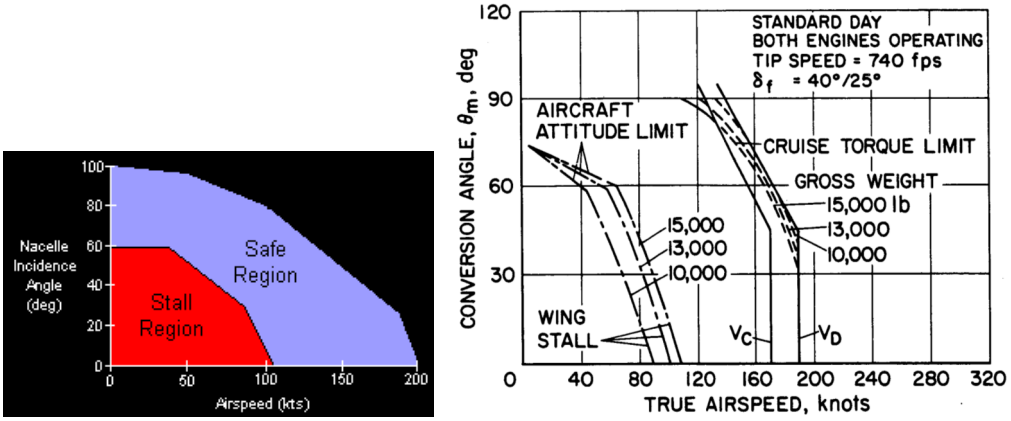

(a) V-22 conversion corridor

(b) XV-15 conversion corridor

Figure 1.5: Conversion corridor examples

Today there are no specific norms regarding the conversion corridor design but future tiltrotor regulations will have to rule and guide also this particular design aspect.

1.2.2 Tiltrotor commands

Piloting a modern tiltrotor is described as quite easy task mainly due to the fly-by-wire control system that acts on control surfaces in such a way that the cyclic lever and pedals movements imply in all conversion phases the same aircraft movements. The XV-15 did not have a fly-by-wire system but a complex mechanism which performs the same function. For example if the pilot pushes the cyclic stick to the right the aircraft rolls right, no matter the flight condition. This may be due to the flaperons moving asymmetrically, it may also be due to asymmetric thrust on the rotors, or it may be a blend of both. The collective lever instead has been differently designed in the different tiltrotors. In the V-22 Osprey a thrust control lever (TCL) moves fore and aft just like an airplane throttle. This lever always controls the rotors thrust acting as a collective in helicopter mode and as a normal thrust lever in airplane mode. The XV-15 and the AW-609 present instead a classical helicopter like collective lever that always controls rotors thrust through rising-lowering movements of the lever.

In all three tiltrotors the nacelles position is controlled through a thumbwheel switch positioned on the thrust command in such a way that the pilot can move it with his left thumb. In the V-22 the pilot can select a certain nacelles angle simply realising the switch in a precise moment. To facilitate the nacelles position control the pilot can visualize on a monitor the actual aircraft position in the conversion corridor. In the XV-15 and AW-609 instead the nacelles are tilted at steps when they are

(a) V-22 thrust control lever (b) AW-609 collective lever

Figure 1.6: Different thrust lever solutions

in the 75° to 0° angle range. A first switch input brings the nacelles from 75° to 50° and a second one brings them to horizontal. This nacelles tilting at steps is called "semi-automatic conversion control". Furthermore in both the V-22 and the AW-609 there are automatic systems that can change the nacelles rotation speed to avoid an accidental aircraft exit from the conversion corridor.

1.3 Thesis purpose and structure

This work aims at developing a numerical methodology to decide which one is the best path within the conversion corridor that should be followed during a conversion from helicopter mode to airplane mode and vice-versa. In order to design such methodology it has been decided to apply it to a classical titlrotor model, the Bell XV-15, for which a large database of information is public available.
To model in an appropriate way the tiltrotor dynamics in any flight condition included within the conversion corridor a complex nonlinear dynamic model should be considered. However, such a model would be difficult to develop and validate, but also very complex to be employed for the synthesis of the controller that should guide the conversion. For these reasons a different approach based on the Linear Parameter-Varying technique has been chosen.
Using a LPV approach a generic nonlinear system:

$$\begin{aligned} \dot{x} &= F(x,u) \\ y &= G(x,u) \end{aligned} \tag{1.1}$$

can be approximate locally about a specific trajectory ($\tilde{x}(t)$,$\tilde{u}(t)$,$\tilde{y}(t)$) by the following linear time-varying system:

$$\begin{aligned} \delta\dot{x} &= \nabla_x F(\tilde{x},\tilde{u})\delta x + \nabla_u F(\tilde{x},\tilde{u})\delta u \\ \delta y &= \nabla_x G(\tilde{x},\tilde{u})\delta x + \nabla_u G(\tilde{x},\tilde{u})\delta u \end{aligned} \tag{1.2}$$

with $\delta u = u - \tilde{u}$, $\delta y = y - \tilde{y}$, $\delta x = x - \tilde{x}$.
For investigation of the LPV capability to be representative of a nonlinear system see [13].

To simulate a conversion manoeuvre it's necessary to define a virtual pilot able to apply the appropriate controls. In the first thesis part this virtual pilot is designed and coupled with aircraft linear models to form a grid of closed-loop pilot-aircraft LTI systems that covers all the conversion corridor envelope. These closed-loop models are then linearly interpolated using the LPV technique to form a nonlinear like model that approximates the aircraft dynamics over the whole conversion corridor. The second part of the thesis uses these closed-loop models collection to find the optimal conversion manoeuvre depending on the objective.

The work start data is a linearized models database of the XV-15 tiltrotor developed using the CAMRAD/JA software. The models database is a collection of state-space models that covers the whole conversion corridor envelope. Each model comes with its trim data allowing to know the trim conditions used in the linearization.

The LQI controllers designed in this work represent the pilot stabilization task assisted by SAS and the pilot tracking task during conversion. The LQI technique adopted allows through weights tuning to contain the control power. It must be stressed that the objective of this control strategy is not the creation of a detailed pilot model, but rather of a controller able to stabilize the aircraft and track a required input signal in a way considered feasible by a typical helicopter pilot.

Consulting different data sources like the XV-15 familiarization document [6], some XV-15, V-22 and AW-609 flight test reports [7],[8],[9],[10] it has been possible to reconstruct a *typical conversion manoeuvre*. During this manoeuvre nacelles are tilted in subsequent steps commanded by the pilot who has also the task to regulate the aircraft airspeed in order to stay within the conversion corridor boundaries.
As figure of merits to drive the conversion manoeuvre optimizations have been chosen quantities like rotor blades flapping angles, safety, pilot workload and conversion time. A schematic of the optimization procedure is reported in figure 1.7.

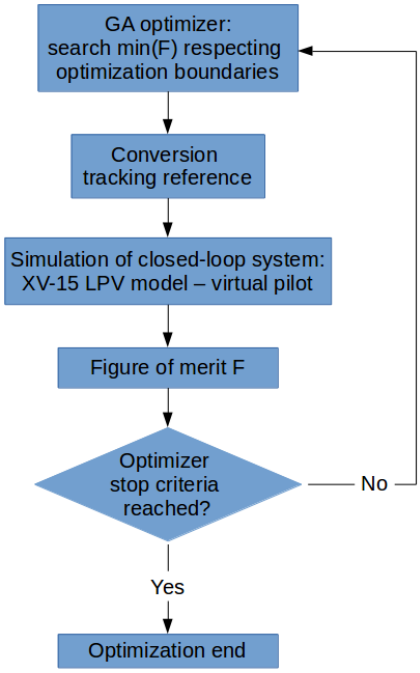

Figure 1.7: Conversion manoeuvre optimization flow chart

Chapter 2

Aircraft linear models database

2.1 Aircraft linear models

A set of state-space models of the aircraft that covers all the conversion corridor was available from previous work. These models have been obtained from Acree and Ferguson reports [2],[3],[4] using CAMRAD/JA, a software dedicated to aerodynamic and dynamic study of rotorcrafts.
In [2] Acree studies the causes of CAMRAD mispredictions on rotor aeroelastic stability and loads relative to the introduction of new composite rotor blades to enhance the XV-15 performance. The report documents the revisions applied to the blade and mechanical control analytical models and discusses their effects on CAMRAD aeroelastic stability predictions for airplane mode flight. In the last part of the report a XV-15 CAMRAD model limited to the airplane configuration is documented. The missing aerodynamic data relative to helicopter and conversion mode are recovered from [3]. In this work Ferguson documents a mathematical model of a generic tiltrotor aircraft designed for real time flight simulations. The data available in this document were used to complete the XV-15 CAMRAD model extending it also to the helicopter and conversion flight modes. In [4] Ferguson validates the mathematical model of a generic tiltrotor through a comparison with flight test data. Through this data and a similar validation work it has been possible to verify the fidelity of the XV-15 CAMRAD model reconstructed from [2] and [3].

An XV-15 state-space model that locally represents the aircraft dynamics about a trim point is described by the following equations:

$$\begin{aligned} \dot{x} &= A(\tilde{x}, \tilde{u}), t)x + B(\tilde{x}, \tilde{u}), t)u \\ y &= C(\tilde{x}, \tilde{u}), t)x \end{aligned} \tag{2.1}$$

where:

$$A(\tilde{x}, \tilde{u}, t) = A(\tilde{x}, \tilde{u}, t + \tau)$$
$$B(\tilde{x}, \tilde{u}, t) = B(\tilde{x}, \tilde{u}, t + \tau)$$
$$C(\tilde{x}, \tilde{u}, t) = C(\tilde{x}, \tilde{u}, t + \tau)$$

Therefore equations 2.1 represent a linear time periodic system, that is such because of the periodicity of rotor blade aerodynamics on a rotor revolution. Being the low aircraft frequency behaviour the objective of this work it's possible to approximate the rotor blades aerodynamic averaging it on the rotor revolution time T_r:

$$\begin{aligned} A(\tilde{x}, \tilde{u}) &= \frac{1}{T_r} \int_0^{T_r} A(\tilde{x}, \tilde{u}, t)\, \mathrm{d}t \\ B(\tilde{x}, \tilde{u}) &= \frac{1}{T_r} \int_0^{T_r} B(\tilde{x}, \tilde{u}, t)\, \mathrm{d}t \\ C(\tilde{x}, \tilde{u}) &= \frac{1}{T_r} \int_0^{T_r} C(\tilde{x}, \tilde{u}, t)\, \mathrm{d}t \end{aligned} \tag{2.2}$$

The XV-15 is provided of two gimbal stiff-in-plane rotors. This rotors characteristic imply sufficiently high in plane frequencies that in this first study can be neglected. Also the first elastic flapping mode is at a relative high frequency and it can be neglected too. However these degree of freedom may be added at later stage for more accurate analysis. The XV-15 gimbal rotor has the layout reported in figure 2.1(a). In this figure is possible to see the particular blades pitch control solution adopted in this rotor: the collective pitch motion is realized through a spider head actioned by a collective tube while the longitudinal pitch is realized separately by a cyclic tube. A specific schematic of the rubber hub spring is reported in figure 2.1(b).

Every linearized XV-15 model has been calculated at the following trim conditions:

- maximum gross weight of 13000 lb
- SLS (Sea Level Standard, ISA)
- null flight path angle γ
- flaperons and flaps inclined according to the flight condition, as shown in figure 2.2

Examples of trim vectors are reported in appendix C.

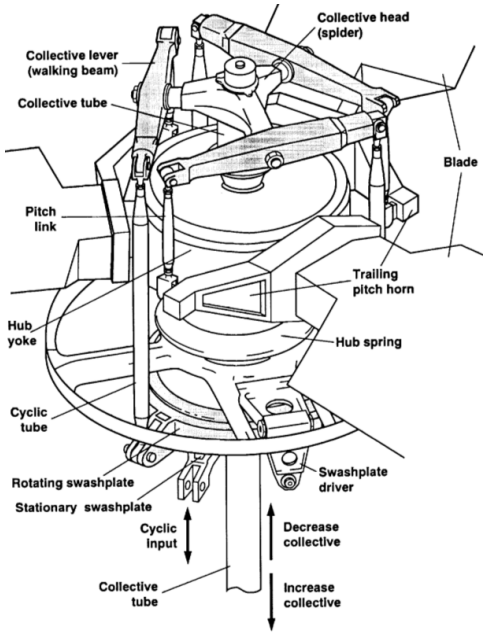

(a) Symplified arrangement of the XV-15 rotor control system (a complete set of control tubes is shown for only one blade)

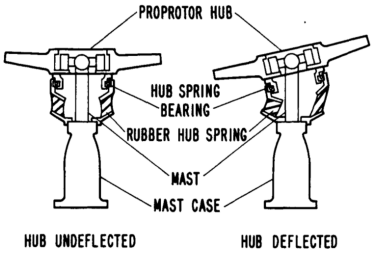

(b) XV-15 hub spring schematic

Figure 2.1: XV-15 rotor

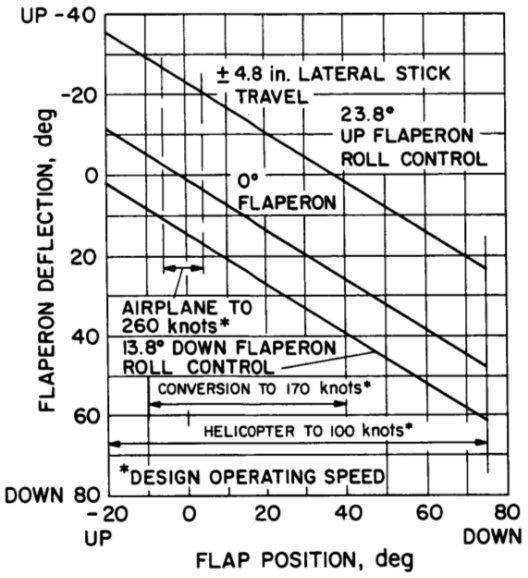

Figure 2.2: Flaperons deflection versus flap position

The modes used to model the aircraft low frequency dynamics are those reported in table 2.1.

State symbol	**State number**	**State description**	**Measure unit**
X_R	X(1:1:5)	Rotor states (multiblade coordinates)	
	X(1)	Collective pitch	rad
	X(2)	Cosine cyclic pitch	rad
	X(3)	Sine cyclic pitch	rad
	X(4)	Cosine cyclic gimbal	rad
	X(5)	Sine cyclic gimbal	rad
θ	X(6)	Airframe pitch attitude	rad
$\dot{X}_R$	X(7:1:11)	dX(1:5)/dt rotor states derivatives	rad/s
$\dot{\theta}$	X(12)	Airframe pitch attitude derivative	rad/s
V_x	X(13)	Airframe fore/aft speed	ft/s
V_z	X(14)	Airframe vertical speed	ft/s
P_v	X(15)	Aircraft altitude	ft

Table 2.1: Linearized models state list

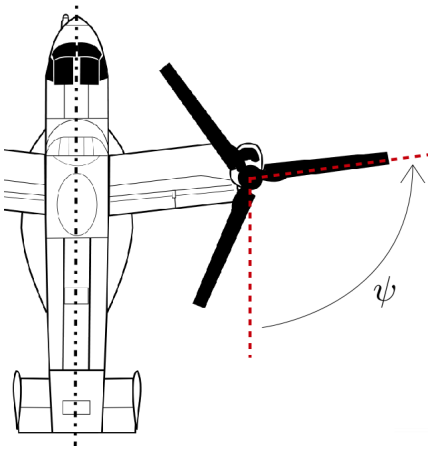

Figure 2.3: ψ azimuth coordinate

Only half of the aircraft has been considered in the dynamic modelling assuming that the aircraft is substantially symmetric. The rotor modes reported are those at lower frequency and are all rigid modes. The flight mechanics modes has been reduced to three because this work considers only symmetric manoeuvres discarding then the antisymmetric aircraft motions.
The first five states regard the right rotor and they are referred to multiblade co-

ordinates allowing for a time invariant description of rotor blades pitch and flapping. X(1) represents the collective blades pitch, where collective indicates that all blades pitch increase when X(1) increase. A positive X(2) represents a positive blade pitch when the blade is at $\psi = 0°$ and a negative pitch when the blade is at $\psi = 180°$ corresponding then to a forward tilting of the swashplate (see figure 2.3 for azimuth coordinate ψ). A positive X(3) represents a positive blade pitch when the blade is at $\psi = 90°$ and a negative pitch when the blade is at $\psi = 270°$ corresponding then to a left tilting of the swashplate. A positive X(4) represents a forward Tip-Path-Plane (TPP) inclination, therefore an upward flapping of the rear blade and a downward flapping of the fore blade. A positive X(5) represents a left TPP inclination, therefore an upward flapping of the right blade and a downward flapping of the left blade. The same applies to the left rotor, taking into account that it rotates in the opposite direction of the right rotor. States from seven to eleven are the time derivatives of the modes just exposed. The rigid rotor modes considered are the minimum rotor states set necessary to control the aircraft and to study rotors blades flapping. States six and twelve represent respectively the aircraft attitude and its time derivative. States thirteen and fourteen are the time derivatives of the airframe forward and vertical displacements expressed in body axes. Body axes reference has its center in the aircraft center of gravity, the X axis points toward aircraft nose, Y axis points toward right wing tip and Z axis points downward.
State fifteen is instead expressed in earth coordinates and it measures the aircraft distance from the ground (aircraft altitude). This last state is used as a sensor allowing to know the aircraft altitude during simulations and it's also used in one LQI feedback loop, as will be shown later. The aircraft altitude state is obtained through the pseudo-integration of the aircraft vertical speed V_v (V_v vector is always perpendicular to the ground and has an upward positive versus):

$$\dot{P_v} = -\tau P_v + V_v \tag{2.3}$$

The τ constant has been used to place the integration pole not exactly in the origin of the complex plane but slightly at it's left, realizing a pseudo-integrator useful to avoid numeric integration problems. V_v in eq. 2.3 is the linear approximation of the vertical speed at trim points, which is calculated as in eq. 2.4:

$$V_v \simeq V_0\theta + \sin(\theta_0)V_x - \cos(\theta_0)V_z \tag{2.4}$$

where V_0 is the aircraft airspeed and θ_0 is the aircraft pitch at trim points.
The original state-space models have three inputs which are reported in table 2.2.

The first two inputs acts on the rotors blades pitch while the third input regulates the elevator deflection. A brief commands explanation follows:

Input number	Input description	Measure unit
u(1)	Collective angle	rad
u(2)	Longitudinal cyclic angle	rad
u(3)	Elevator angle	rad

Table 2.2: Initial state-space inputs

- u(1) modifies the rotor blades pitch collectively, so that corresponds to a vertical translation of the swashplate. A positive u(1) corresponds to a rising (positive - see figure 2.4(a) for pilot commands conventions) collective lever displacement.
- u(2) acts on the pitch blades at $\psi = 90°$ and $\psi = 270°$, corresponding to a lateral swashplate inclination. This command imply a backward TPP inclination and therefore corresponds to a displacement toward the pilot (negative - see figure 2.4(b)) of the cyclic stick.
- u(3) represents the elevator deflection. A positive u(3) indicates a downward rotation of the elevator corresponding therefore to a diving (positive) cyclic stick command.

As this work focuses on the conversion manoeuvre that happens in the plane of symmetry of the aircraft the lateral cyclic inputs that generate aircraft movements outside the plane of symmetry are not considered. Differential flaperon inputs together with the differential collective and cyclic commands have not been taken into consideration for the same reason.

2.1.1 Control chain flexibility

The swashplate commands are realized imposing a certain swashplate inclination through hydraulics actuators. Only the *rigid* collective and cyclic pitch blade modes are considered in this work, neglecting the blades pitch torsion. Therefore the control chain flexibility it's here intended as the flexibility in the pitch links. The aircraft models used in this work take into account this characteristic providing for each trim condition the collective pitch gap from the swashplate command u(1) and the blades collective pitch angle X(1). This last is calculated as:

$$X(1) = u(1) + \Delta_f \quad [rad] \tag{2.5}$$

In appendix B are reported the Δ_f values (expressed in degrees) on trim points. It's important to remind that Δ_f is representative of the gap between u(1) and X(1) only in the static trim conditions in which is calculated.

2.2 Pilot commands gains and biases

Swashplate commands are now translated to pilot stick inputs. This allows later on the study of the pilot stick displacement histories during the conversion manoeuvre. In chapters that follow commands **u** refer to the collective lever displacement and to the longitudinal displacement of the cyclic stick, respectively u_{COLL} and u_{CYCL}. The sticks positive displacement conventions are reported in figure 2.4.

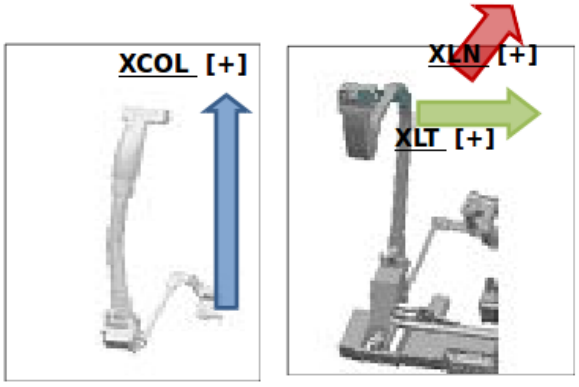

(a) Collective sign convention (b) Cyclic sign convention

Figure 2.4: Pilot stick conventions

In table 2.3 command stops of interest are reported.

Command	MIN [in]	MAX [in]
u_{COLL}	0	10
u_{CYCL}	-4.8	4.8

Table 2.3: Minimum and maximum commands excursion

During conversion the aerodynamic of the tiltrotor undergo great modifications having the aircraft to radically switch from a helicopter to an airplane configuration. To deal with this aerodynamic modifications major changes in the aircraft configuration take place. To cite a few: flaperons deflection goes from 47° max deflection to 0°, rotors blades pitch goes from a approximately 10° (at maximum GW, SLS) in hover to about 35° in airplane mode at cruise speed and once in airplane mode rotors rotation frequency goes from 565 (100%) to 458 (80%) RPM and . Additionally, while the collective stick always control rotors thrust in both helicopter and airplane mode, the longitudinal motion of the cyclic stick controls the cyclic pitch *and* the elevator in all conversion phases except in airplane mode where only the elevator surface is controlled by this pilot command. Therefore there is the need for different

ψ [deg]	0	30	60	75	90
K0CFE [deg/in]	5.264	4.971	2.805	2.389	1.837
KSCFE [deg/in]	0	1.040	1.810	2.035	2.100
KECFE [deg/in]	4.735	4.735	4.735	4.735	4.735

Table 2.4: Input gains

gains from the control sticks to swashplates and elevator during the conversion. There's also the need to introduces biases. For example if one looks at the rotor blades pitch variation during the whole conversion manoeuvre it increase of about 25°. This would imply the collective lever to constantly rise during conversion, ending in airplane mode with a great displacement of the lever. For ergonomic reasons is not desirable to keep the control lever in the upper position during airplane cruise, so to re-set its position a bias/offset has to be introduced.
Figure 2.5 compares the collective pitch mode X(1) with collective lever position during a typical conversion manoeuvre showing how bias introduction allow for a lowered collective stick end position.

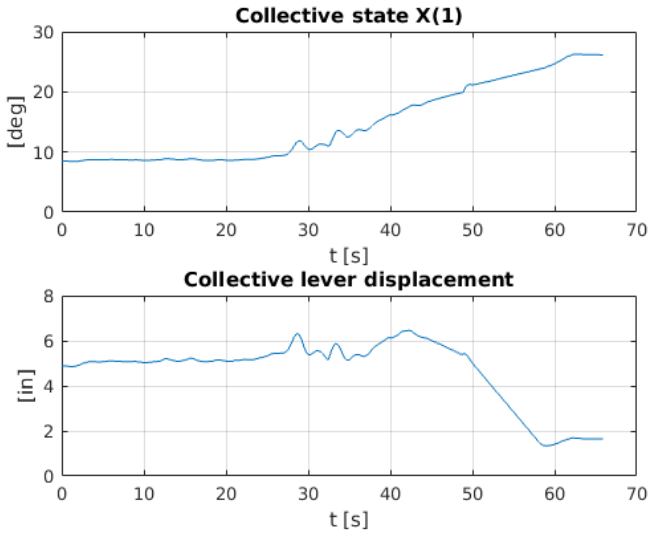

Figure 2.5: Collective pitch mode X(1) and collective lever position u_{COLL} trends

The introduced biases allow also for a centered cyclic stick position at the end of the conversion. Figure 2.6 compares the longitudinal pitch mode X(3) with the longitudinal cyclic stick position during a typical conversion manoeuvre. A summary of gains and biases used for calculate pilot inputs is reported respectively in table 2.4 and 2.5.

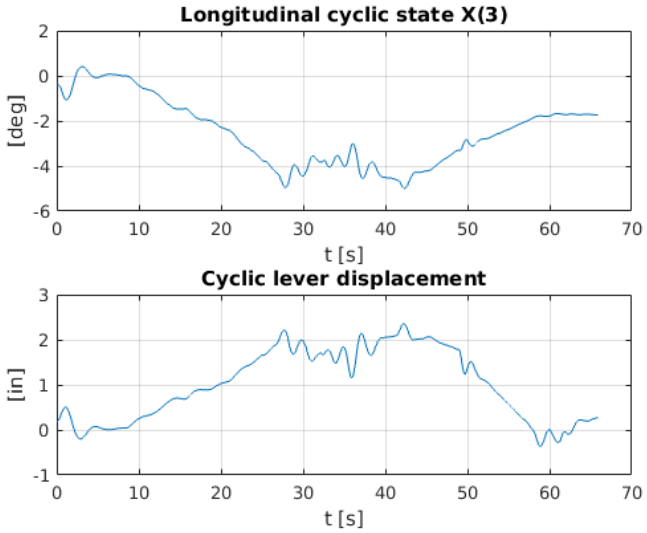

Figure 2.6: Longitudinal pitch mode X(3) and longitudinal cyclic stick position u_{CYCL} trends

ψ [deg]	0	30	60	75	90
θ_0 [deg]	21.300	-3.185	0.000	0.000	2.900
θ_{1s} [deg]	-1.5	-0.75	-0.2	-0.05	0
δ [deg]	0	0	0	0	0

Table 2.5: Input biases

Availing of the gains table it's possible to express swashplate inputs into pilot stick displacements. The conversion from blades pitch / elevator rotation inputs to stick displacement inputs depends on nacelles angle ψ_n through the conversion matrix 2.6.

$$T(\psi_n) = \begin{bmatrix} K_{0CFE}(\psi_n) & 0 \\ 0 & -K_{SCFE}(\psi_n) \\ 0 & K_{ECFE}(\psi_n) \end{bmatrix} \frac{\pi}{180} \tag{2.6}$$

The new B matrix that receives pilot displacement commands in inches is:

$$B = \overline{B} \cdot T \tag{2.7}$$

where $\overline{B}$ stays for the original B matrix.

2.3 Aircraft models distribution on conversion corridor

The conversion manoeuvre can be executed following different corridor pathways. Potentially the conversion path can span throughout the whole corridor. Therefore the tiltrotor dynamics has to be described by a sufficiently dense grid of LTI models that lays within the corridor boundaries. Several tries has been necessary to tune the models grid density in such a way that the models collection could effectively represent the aircraft non-linear behaviour. The models resolution in the airspeed V variable has been chosen checking the trim error between one model and the model at the successive airspeed grid value considering the same nacelles angle. To the model at lower speed has been imposed a V reference corresponding to the airspeed gap from the successive model. Once the model reached a static trim condition at the airspeed required a check between the model states and the successive model trim made possible to understand the amount of error due to linearization. The chosen models resolution is of 10 Kn, with the addition of a model at 5 Kn in helicopter mode to better simulate the transition from hover to forward flight. A similar method has been used to choose the models grid resolution in the nacelles angle ψ_n variable: in this case the airspeed has been kept constant and the nacelles angle has been varied. An adequate ψ_n resolution has been judge to be:

$$\psi_{n\ Models} = \{\ 0^\circ\ 30^\circ\ 60^\circ\ 75^\circ\ 90^\circ\ \}$$

Figure 2.7 represents the conversion corridor and the models available.

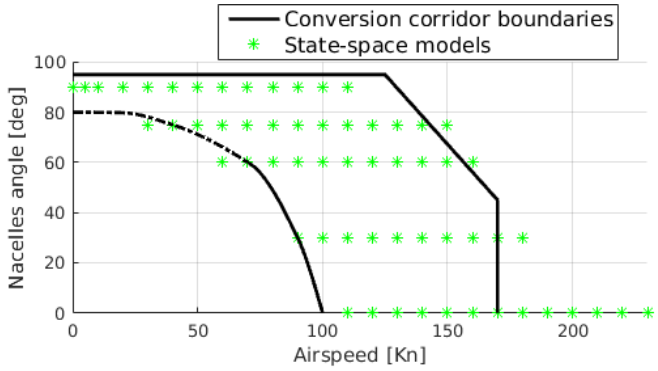

Figure 2.7: State-space models on the conversion corridor

Two models at upper right and one model at lower left corner of the conversion corridor are missing (see fig. 2.7) because it wasn't possible to trim the CAMRAD/JA XV-15 model under these conditions of speed and nacelles angle.
The conversion corridor is delimited by four curves (in thick black in figure 2.7). The upper boundary is the horizontal line at 95° nacelles angle, corresponding to

the backward nacelles stops. The lower boundary is the 0° nacelles angle, that represents the aircraft in airplane configuration with nacelles locked in down-stops.
The left and right boundaries are limits on the aircraft speed. The left corridor border defines the aircraft stall speed although the upper part of this curve (from 90° to 60° nacelles angle, dotted in figure 2.7) doesn't exactly represent the stall limit. In fact, at the immediate right of this upper curve part, the wing is still not producing sufficient lift.
The right line define the cruise speed V_C here considered as practical conversion high speed limit. In fact the V_D curve has a right offset of only 20 Kn with respect to V_C and it's not reachable from 90° to 45° nacelles angle because of the transmission torque limit.
The boundaries just described and reported in figure 2.7 are the approximation of the curves at 13000 lb GW reported in figure 1.5(b), from [6].

Chapter 3

Virtual pilot design

3.1 Virtual pilot modelling

The modelling of pilot control behaviour starts in the 1940's [14] with studies on the human operator. From then until the 1960's, research was focused on model the human as a controller of single-input/single-output systems using frequency domain models [15]. Since the 1960's, part of the research has concentrated on the analysis of multivariate systems using time domain methods and optimization theory. The Optimal Control Model (OCM) proposed by Kleinman, Baron and Levison in 1970 [16], [17] has been the first attempt to describe the behaviour of the human pilot in a time domain optimal control framework. The OCM basic assumption is that the well-trained and careful human controller behaves optimally in some sense, adjusting the pilot's compensation for a given vehicle and task. The OCM has been widely used and has been validated in several tasks.
The pilot model implemented in this thesis work is derived from the Modified Optimal Control pilot Model (MOCM) [1] which is an improved version of the OCM. The MOCM retains the key aspects of the OCM such as a linear quadratic solution for the pilot gains with inclusion of control rate in the cost function, a Kalman estimator, and the ability to account for attention allocation and perception threshold effects. However, unlike the OCM, the structure of this model allows for direct calculation of pilot and system transfer functions.
In this thesis work a simplified MOCM scheme has been implemented. The Kalman filter design has been discarded and a full-state feedback control law has been adopted. This imply the renunciation to model a realistic and precise virtual pilot which among the others loose the capability to take into account for attention allocation and perception threshold effects but it greatly simplifies the controller design. This work aims in fact not to model a realistic pilot behaviour but to realize a virtual pilot that can stabilize the aircraft and perform tracking tasks imparting commands

replicable by a real helicopter pilot. A classical optimal control design would consist of a Linear-Quadratic-Regulator (LQR) to stabilize the aircraft and of Proportional-Integral-Derivative (PID) controllers to track the reference signals. However, in this work these control functions are both carried out by an LQI controller, which is designed following the guidelines of the MOCM.

3.2 The Linear-Quadratic-Integral control

The Linear-Quadratic-Integral (LQI) control is a control technique that allows the stabilization and tracking of a Multi-Input-Multi-Output (MIMO) dynamic system. LQI computes an optimal state-feedback control law for the tracking loop shown in figure 3.1. An infinite-horizon, continuous-time LQI regulator has been designed for

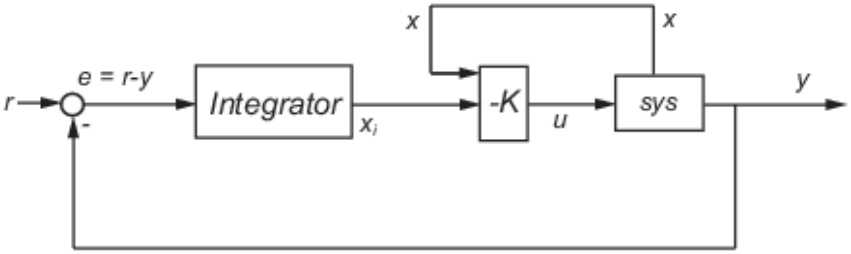

Figure 3.1: LQI control scheme

each LTI model available. In general, for a plant with the state-space equations:

$$\begin{aligned} \dot{x} &= Ax + Bu \\ y &= Cx + Du \end{aligned} \tag{3.1}$$

and with a cost functional defined as:

$$J = \int_0^\infty (x^T Q x + u^T R u + 2x^T N u)\,\mathrm{d}t \tag{3.2}$$

the feedback control law that minimizes the value of the cost is:

$$u = -K\ [x; x_i] \tag{3.3}$$

where x_i is the integrator output. This control law ensures that the output y tracks the reference command r. For MIMO systems, the number of integrators equals the dimension of the output y.
The gain matrix K is given by:

$$K = R^{-1}(B^T P + N^T) \tag{3.4}$$

and P is found by solving the continuous time algebraic Riccati equation:

$$A^T P + PA - (PB + N)R^{-1}(B^T P + N^T) + Q = 0 \tag{3.5}$$

3.3 Controllers desing

To track signals with commands that can be executed by a real pilot it's necessary to control the system in commands derivatives. In this way it's possible to restrain the maximum command derivatives via a correct setting of input weights in the R matrix, as shown later. In figure 3.2 it's reported the control scheme implemented. The

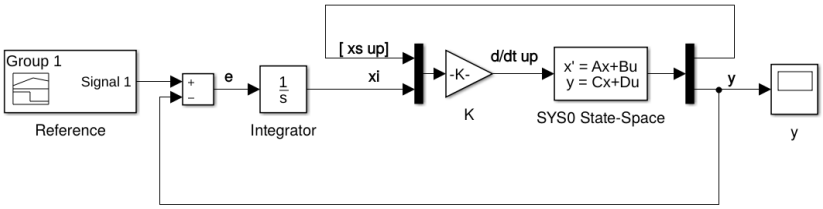

Figure 3.2: LQI scheme implemented

pilot's effective time delay is modelled by a second-order Padé approximation because it provides a good approximation to a pure delay over the pilot's frequency range of interest (that range approximately from 0.1 to 10 rad/s). The pilot's effective time delay is placed at each pilot's output and is treated as part of the plant dynamics for determination of the pilot's regulation gains.
Considering one input channel, a second order Padé approximation has the form:

$$\frac{u_d}{u_p} = \frac{1 - \frac{1}{2}(\tau s) + \frac{1}{8}(\tau s)^2}{1 + \frac{1}{2}(\tau s) + \frac{1}{8}(\tau s)^2} \tag{3.6}$$

where τ is the delay interval (in seconds), u_p is one pilot's input, and u_d is the delayed pilot's output.
In state-space form, this can be expressed by:

$$\begin{aligned} \dot{x}_d &= \widehat{A}_d x_d + \widehat{B}_d u_p \\ \delta = u_d &= \widehat{C}_d x_d + u_p \end{aligned} \tag{3.7}$$

where x_d is a two-element vector of Padé delay states.

Pilot's inputs are the collective and cyclic levers, so a delay block for each input channel is needed. The parallel of these two delay blocks has the following state-space representation:

$$\dot{x}_d = \begin{bmatrix} \widehat{A}_d & 0 \\ 0 & \widehat{A}_d \end{bmatrix} x_d + \begin{bmatrix} \widehat{B}_d & 0 \\ 0 & \widehat{B}_d \end{bmatrix} u_p$$
$$y = \begin{bmatrix} \widehat{C}_d & 0 \\ 0 & \widehat{C}_d \end{bmatrix} x_d + \begin{bmatrix} 1 & 0 \\ 0 & 1 \end{bmatrix} u_p$$

or:

$$\left.\begin{aligned} \dot{x}_d &= A_d x_d + B_d u_p \\ \delta = u_d &= C_d x_d + u_p \end{aligned}\right\} \text{ Sys}_d \tag{3.8}$$

where x_d is now a four element vector of Padé delay states.

The tiltrotor system augmented with pilot's effective time delay is represented by Sys_s:

$$\frac{d}{dt}\begin{Bmatrix} x \\ x_d \end{Bmatrix} = \begin{bmatrix} A & BC_d \\ 0 & A_d \end{bmatrix} \begin{Bmatrix} x \\ x_d \end{Bmatrix} + \begin{bmatrix} B \\ B_d \end{bmatrix} u_p$$
$$y = \begin{bmatrix} C & DC_d \end{bmatrix} \begin{Bmatrix} x \\ x_d \end{Bmatrix} + Du_p$$

or:

$$\left.\begin{aligned} \dot{x}_s &= A_s x_s + B_s u_p \\ y &= C_s x_s + D_s u_p \end{aligned}\right\} \text{ Sys}_s \tag{3.9}$$

The system 3.9 can be expressed in a control-rate formulation by defining a new state vector:

$$x_r = [x_s;\ u_p]$$

Then the control-rate formulation of 3.9 is:

$$\frac{d}{dt}\begin{Bmatrix} x \\ x_d \\ u_p \end{Bmatrix} = \begin{bmatrix} A & BC_d & B \\ 0 & A_d & B_d \\ 0 & 0 & 0 \end{bmatrix} \begin{Bmatrix} x \\ x_d \\ u_p \end{Bmatrix} + \begin{bmatrix} 0 \\ 0 \\ I \end{bmatrix} \dot{u}_p$$
$$y = C_r \begin{Bmatrix} x \\ x_d \\ u_p \end{Bmatrix}$$

or:

$$\left.\begin{aligned}\dot{x}_r &= A_0 x_r + B_0 \dot{u}_p \\ y &= C_0 x_r\end{aligned}\right\} \text{ Sys}_0 \tag{3.10}$$

where C_r selects as output the vertical position state P_v and the linear approximation of the aircraft airspeed V. Therefore C_r is:

$$\mathbf{C_r} = \begin{array}{c} \begin{array}{cccccc} x(1:22) & V_x & V_z & P_v & x_d & u_p \end{array} \\ \begin{pmatrix} 0 & 0 & 0 & 1 & 0 & 0 \\ 0 & \cos(\theta_0(i)) & \sin(\theta_0(i)) & 0 & 0 & 0 \end{pmatrix} \end{array} \tag{3.11}$$

In fact, the linearization of V at trim points can be calculated as in eq. 3.12:

$$V \simeq \cos(\theta_0) V_x + \sin(\theta_0) V_z \tag{3.12}$$

where θ_0 is the aircraft pitch at trim points.

The LQI solution technique is now applied to the augmented system 3.10 leading to the control scheme initially reported in figure 3.2. As can be seen from this figure, the tracking states x_i are:

$$x_i = \frac{1}{s} e = \frac{1}{s}(r - y) = \frac{1}{s}(r - C_r x_r) \tag{3.13}$$

or:

$$\dot{x}_i = r - C_r x_r \tag{3.14}$$

It can now be defined a new state vector:

$$\chi = \begin{Bmatrix} x \\ x_d \\ u_p \\ x_i \end{Bmatrix} = \begin{Bmatrix} x_s \\ u_p \\ x_i \end{Bmatrix}$$

It's assumed that the pilot control task can be defined by the minimization of the quadratic performance index J_p given by:

$$J_p = E_\infty \{\chi^T Q \chi + \dot{u}_p^T R \dot{u}_p\} \tag{3.15}$$

with cost functional weightings $Q \geq 0$, $R > 0$. It has to be noted that in the functional J_p just defined there is no N matrix that it's assumed to be null.

Accordingly to the LQI technique the minimizing control law is obtained by the full-state feedback relation:

$$\dot{u}_p = -K\chi \tag{3.16}$$

The system closed-loop eq.s are:

$$\frac{d}{dt}\begin{Bmatrix} x_s \\ u_p \\ x_i \end{Bmatrix} = \begin{bmatrix} A_s & B_s & 0 \\ 0 & 0 & 0 \\ -C_r & & 0 \end{bmatrix} \begin{Bmatrix} x_s \\ u_p \\ x_i \end{Bmatrix} + \begin{bmatrix} 0 \\ I \\ 0 \end{bmatrix} \dot{u}_p + \begin{bmatrix} 0 \\ 0 \\ I \end{bmatrix} r \tag{3.17}$$

Substituiting 3.16 eq.s 3.17 become:

$$\begin{gathered} \frac{d}{dt}\begin{Bmatrix} x_s \\ u_p \\ x_i \end{Bmatrix} = \begin{bmatrix} A_s & B_s & 0 \\ & -K & \\ -C_r & & 0 \end{bmatrix} \begin{Bmatrix} x_s \\ u_p \\ x_i \end{Bmatrix} + \begin{bmatrix} 0 \\ 0 \\ I \end{bmatrix} r \\ u_d = C_\delta \begin{Bmatrix} x_s \\ u_p \\ x_i \end{Bmatrix} \end{gathered} \tag{3.18}$$

where C_δ is:

$$\mathbf{C}_\delta = \begin{matrix} x & x_d & u_p & x_i \end{matrix} \begin{pmatrix} 0 & C_d & 1 & 0 \end{pmatrix} \tag{3.19}$$

3.4 Pilot controller subpart

The virtual pilot behaviour part of the controllers can be spotted rearranging the gain matrix K just calculated. Matrix K can be ideally column splitted into three sub-matrixes:

$$\mathbf{K} = \begin{matrix} x_s & u_p & x_i \end{matrix} \begin{pmatrix} K_s & K_p & K_i \end{pmatrix} \tag{3.20}$$

K_p it's taken apart to constitute the *neuro-motor lag block* (see figure 3.3) while the remaining gains matrixes K_s and K_i form the following new gain matrix:

$$K_{si} = [K_s \; K_i] \tag{3.21}$$

With these manipulations the control scheme 3.2 becomes as in figure 3.3. In fact, expanding the optimal control law 3.16 using this K subdivision just introduced one obtains:

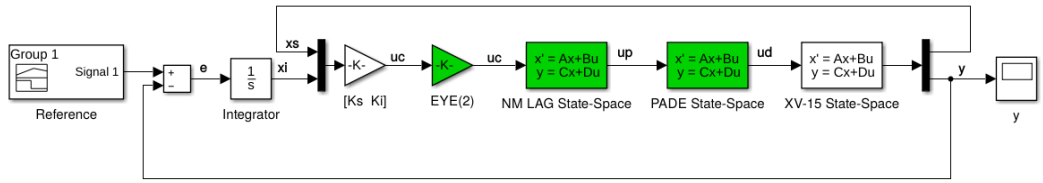

Figure 3.3: Re-organised LQI control scheme.
The virtual pilot constituted by green blocks

$$\dot{u}_p = -(K_s x_s + K_p u_p + K_i x_i) \tag{3.22}$$

Defining the pilot commanded control u_c:

$$u_c = -K_p^{-1}(K_s x_s + K_i x_i)$$

Eq. 3.22 can be written as:

$$\dot{u}_p = -K_p u_p + K_p u_c \tag{3.23}$$

Then the following neuro-motor lag state-space system can be defined:

$$\left.\begin{aligned} \dot{u}_p &= -K_p u_p + K_p u_c \\ y &= I u_p \end{aligned}\right\} \ \mathrm{Sys}_{NML} \tag{3.24}$$

Eq.s 3.24 represent the neuro-muscolar pilot dynamics and corresponds to the neuro-motor lag block in figure 3.3. This is a MIMO system with a size two input vector u_c and a size two output vector u_p. Being the K_p diagonal elements larger than extradiagonal elements (in absolute terms) it's possible to approximate the MIMO system 3.24 with two SISO first order systems:

$$\begin{aligned} \dot{u}_{p_1} &= -K_{p_{11}} u_{p_1} + K_{p_{11}} u_{c_1} \\ \dot{u}_{p_2} &= -K_{p_{22}} u_{p_2} + K_{p_{22}} u_{c_2} \end{aligned} \tag{3.25}$$

Figure 3.4 shows that step response differences are very small legitimating the approximation just introduced.

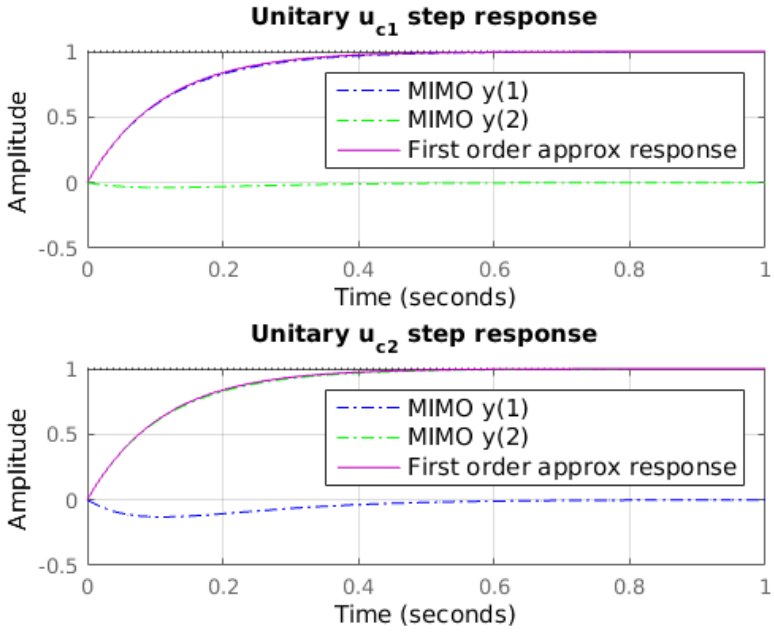

Figure 3.4: Step responses for XV-15 model at 110 Kn, 60° nacelles angle

Then the neuro-motor lag block can be seen as a parallel of two of the following transfer function:

$$\frac{u_{p_1}}{u_{c_1}} = \frac{u_{p_2}}{u_{c_2}} = \frac{1}{sT_N + 1} \tag{3.26}$$

where the neuro-muscolar time constant is:

$$T_N = \frac{1}{K_p} \tag{3.27}$$

It has been shown that the neuro-motor lag block has a first order approximable dynamic. Tuning T_N is then possible to restrain the maximum commands derivatives for a given input u_c obtaining a smooth conversion control history, as in the real case.

Considering one of the two command channels, the final pilot transfer function is:

$$P(s) = K_H \frac{1}{sT_N + 1} e^{-\tau s} \tag{3.28}$$

where:
$K_H = 1$
$T_N = 0.11s$
$\tau = 0.15s$

These pilot parameters are chosen in accordance to the MOCM [1, p. 11] and to standard pilot models like that reported in [5] as *Precision Pilot Model*. Figure 3.5 shows the Bode diagram of the pilot transfer function 3.28.

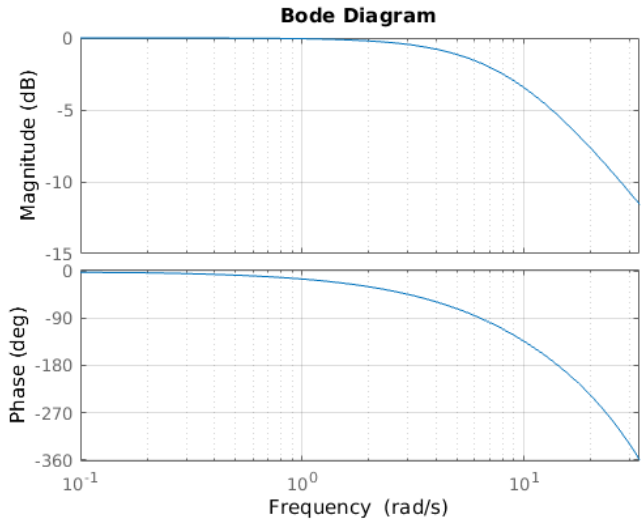

Figure 3.5: Pilot transfer function bode diagram

It's then possible to determine the pilot bandwidth:

$$\omega_{p_{-3dB}} = 9.1 \frac{rad}{s} = 1.5Hz \tag{3.29}$$

The value obtained well represent a real pilot bandwidth.

3.4.1 The whole controller

The whole controller goes from the input vector $[xs; xi]$ to the output vector u_d in figure 3.3 and therefore corresponds to the blue blocks collection in figure 3.6.

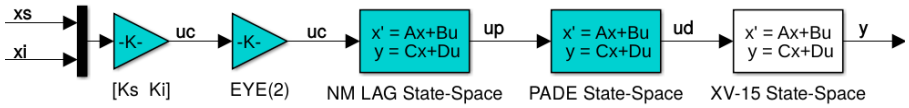

Figure 3.6: Complete controller scheme

The state-space equations of the controller reported in figure 3.6 are:

$$\begin{aligned} \frac{d}{dt}\begin{Bmatrix} x_d \\ u_p \end{Bmatrix} &= \begin{bmatrix} A_d & B_d \\ 0 & -K_p \end{bmatrix}\begin{Bmatrix} x_d \\ u_p \end{Bmatrix} + \begin{bmatrix} 0 & 0 \\ -K_s & -K_i \end{bmatrix}\begin{Bmatrix} x_s \\ x_i \end{Bmatrix} \\ u_d &= \begin{bmatrix} C_d & I \end{bmatrix}\begin{Bmatrix} x_d \\ u_p \end{Bmatrix} \end{aligned} \tag{3.30}$$

Figure 3.7 shows the commands FFT of the typical conversion manoeuvre, that will be defined in 6.2.

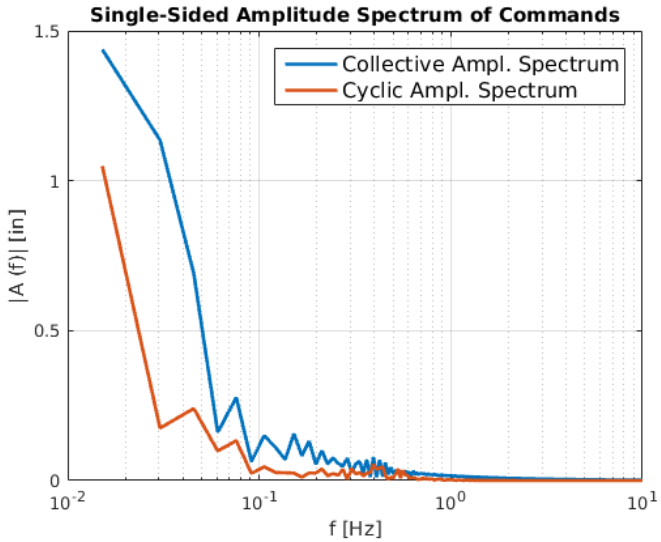

Figure 3.7: Typical conversion manoeuvre commands spectrum

As can be seen the vast majority of commands actuation stays within the pilot bandwidth and it's then executable by a real pilot.

3.5 Cost function parameters

Q and R are diagonal matrixes whose elements need to be tuned to obtain a satisfying control. A weight coefficient in Q represents the importance in maintaining the corresponding state close to zero while a weight coefficient in R represents the

control power limitation on the corresponding input channel.

Normally the parameters in Q and R are determined iteratively until the response of the system under control is satisfying. Q weights have been tuned this way while R weights have been tuned automatically by the $fgoalattain$ multi-objective gradient based optimizer. $fgoalattain$ goals have been set to obtain:

$$K_{p_{11}} = K_{p_{22}} = \frac{1}{T_N} \tag{3.31}$$

Therefore $fgoalattain$ is required to obtain for every LQI controller the following K_p diagonal values:

$$\begin{aligned} K_{p11} &= 9.09 \\ K_{p22} &= 9.09 \end{aligned} \tag{3.32}$$

R is a 2 x 2 diagonal matrix:

$$R = \begin{bmatrix} R_{11} & 0 \\ 0 & R_{22} \end{bmatrix}$$

For each model $fgoalattain$ finds R_{11} and R_{22} that gives the desired K_p diagonal values. R_{11} and R_{22} values are reported in tables 3.1 and 3.2.

Q weights are the same for all designed controllers:

$$\mathbf{diag(Q)} = \begin{array}{c} \begin{array}{cccccccccccc} X_R & \theta & \dot{X_R} & \dot{\theta} & V_x & V_z & P_v & X_d & u_{p_1} & u_{p_2} & x_{i_1} & x_{i_2} \end{array} \\ \begin{pmatrix} 0 & 0 & 0 & 1 & 1 & 0 & 0 & 0 & 1 & 1.5 & 2 & 1 \end{pmatrix} \end{array} \tag{3.33}$$

States not observable by the pilot like rotor states X_R and Padé states X_d have their corresponding Q weights set to zero. The other weights have been tuned to obtain a good pilot tracking performance but also a smooth response, with not to much aggressive pilot commands. These gentle controlling allow to never reach command stops (max displacement) also in the most challenging tracking task.

V [Kn]	$\psi = 90°$	$\psi = 75°$	$\psi = 60°$	$\psi = 30°$	$\psi = 0°$
0	0.0426				
5	0.0424				
10	0.0421				
20	0.0412				
30	0.0408	0.0576			
40	0.0406	0.0556			
50	0.0404	0.0542			
60	0.0400	0.0535	0.1024		
70	0.0395	0.0526	0.0937		
80	0.0391	0.0519	0.0918		
90	0.0388	0.0510	0.0906	0.6508	
100	0.0388	0.0499	0.0886	0.6339	
110	0.0389	0.0492	0.0860	0.6155	1.3020
120		0.0489	0.0834	0.5974	1.3184
130		0.0489	0.0813	0.5824	1.3025
140		0.0651	0.0794	0.5685	1.2929
150		0.0492	0.0781	0.5589	1.2802
160			0.0764	0.5527	1.2754
170				0.5491	1.2719
180				0.5450	1.2725
190					1.2793
200					1.2892
210					1.3009
220					1.3168
230					1.3360

Table 3.1: First diagonal element R_{11}

V [Kn]	$\psi = 90°$	$\psi = 75°$	$\psi = 60°$	$\psi = 30°$	$\psi = 0°$
0	0.0588				
5	0.0585				
10	0.0583				
20	0.0572				
30	0.0540	0.0544			
40	0.0511	0.0545			
50	0.0513	0.0556			
60	0.0538	0.0559	0.0469		
70	0.0590	0.0576	0.0584		
80	0.0680	0.0615	0.0645		
90	0.0818	0.0690	0.0699	0.0652	
100	0.1014	0.0818	0.0797	0.0740	
110	0.1346	0.1040	0.0943	0.0854	0.0643
120		0.1405	0.1158	0.1004	0.0863
130		0.1952	0.1503	0.1211	0.1001
140		0.3805	0.2025	0.1495	0.1161
150		0.3816	0.2785	0.1893	0.1340
160			0.3820	0.2444	0.1575
170				0.3195	0.1855
180				0.4187	0.2143
190					0.2541
200					0.3011
210					0.3573
220					0.4244
230					0.5032

Table 3.2: Second diagonal element R_{22}

Chapter 4

LPV design

4.1 Linear Parameter-Varying (LPV) system

A linear parameter-varying (LPV) system is a linear state-space model whose dynamics vary as a function of certain time-varying parameters called scheduling parameters.

The LPV model is represented in Matlab in a state-space form using coefficients that are parameter dependent. The equations that represent an LPV are:

$$\begin{aligned} dx(t) &= A(p)x(t) + B(p)u(t) \\ y(t) &= C(p)x(t) + D(p)u(t) \\ x(0) &= x_0 \end{aligned} \tag{4.1}$$

where:

- u(t) are the inputs
- y(t) are the outputs
- x(t) are the model states with initial value x_0
- dx(t) is the state derivative vector
- A(p), B(p), C(p) and D(p) are the state-space matrixes parametrized by the scheduling parameter vector p.

In general the parameters $p = p(t)$ are scalar-valued quantities that can be functions of time, inputs, states and constants. In this thesis work two parameters have being used:

- the aircraft airspeed V
- the nacelle angle ψ_n

therefore parameters form a vector of dimension two. The operating space over which the LPV model is defined is constructed by this two continuous variables.

The LPV block in Simulink implements a grid-based representation, meaning that a grid of parameter values has to be consider. In other terms, at each point of the grid the parameter vector assume certain values, for example $p = [V^* \ \psi_n^*]$.
Here V depends on states X(13) and X(14) (V_x and V_z) as can be seen in the linearization 3.12 and it's also function of time. The nacelles angle ψ_n is a reference signal and therefore it's a given function of time. The software then interpolates the values of the scheduling variables through the operating space. Also at each grid point is associated the corresponding linear system as a state-space model object.

To sum up, to define an LPV system one has to define an array of state-space models with operating points information. The information on the scheduling variables is extracted from the SamplingGrid property of the LTI array, where the SamplingGrid property it's in fact a property that tracks the scheduling variable values associated with each model in the array. The scheduling variables define the LPV models grid. Finally the LPV block uses this LTI array with data interpolation and extrapolation techniques for simulation. Figure 4.1 from [5] depict a grid in the two scheduling variables α and V.

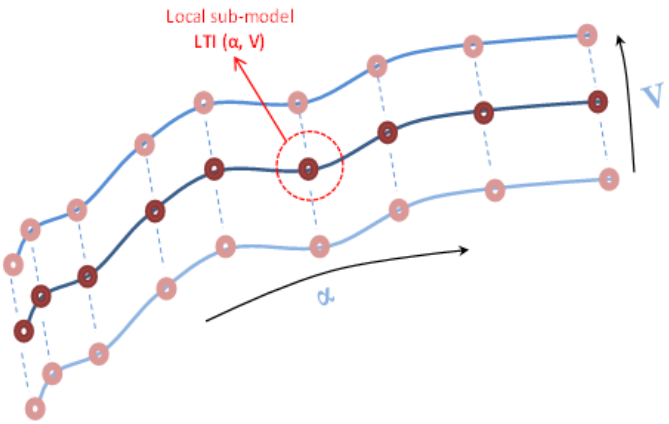

Figure 4.1: Example of a two parameters grid

Each donut in figure 4.1 represents a local LTI model, and the connecting curves represent the interpolation rules. The abscissa and ordinate of the surface are the scheduling parameters (α, V) in this particular example.

Further operating point information can be feeded at each grid point. This additional data are known as offsets in the dx, x, u and y variables. This form that include offset information is known as *affine form* of the LPV model.

The offset extended LPV representation is mathematically described by the following equations:

$$\begin{aligned} \dot{x}(t) &= A(p)x(t) + B(p)u(t) + (\dot{\overline{x}}(p) - A(p)\overline{x}(p) + B(p)\overline{u}(p)) \\ y(t) &= C(p)x(t) + D(p)u(t) + (\overline{y}(p) - C(p)\overline{x}(p) + D(p)\overline{u}(p)) \\ x(0) &= x_0 \end{aligned} \tag{4.2}$$

where $\dot{\overline{x}}(p), \overline{x}(p), \overline{u}(p), \overline{y}(p)$ are the offsets in the values of $\dot{x}(t), x(t), u(t), y(t)$ at a given parameter value $p = p(t)$.
In this work $\dot{\overline{x}}(p)$ is always null due to the XV-15 models static trim conditions. Examples of $\overline{x}(p)$ vectors are reported in appendix C. All LPV input offsets $\overline{u}(p)$ are null 2-by-1 vectors because input vector components are the pilot command derivatives $\dot{u}_{COLL}$ and $\dot{u}_{CYCL}$. $\overline{y}(p)$ are not relevant offsets because V and P_v quantities has been non-linearly recomputed with Simulink blocks starting from states values, as explained in section 5.1.

4.2 LPV interpolation and extrapolation

When the scheduling parameters are located away from their grid locations an interpolation of the state-space models and offsets is made by the LPV block. There are three different interpolation methods available:

- *flat*: choose the state-space and offset data at the grid point closest, but not larger than, the current point. The current point is the value of the scheduling parameters at current time p(t*);
- *nearest*: choose the state-space and offset data at the closest grid point in the scheduling space;
- *linear*: obtain state-space and offset data by linear interpolation of the nearest 2d neighbors in the scheduling space, where d is the number of scheduling parameters. In this work $d = 2$.

Figure 4.2 shows these three different interpolation types comparing the actual pitch θ of the tiltrotor to the interpolated θ offset. The tracking task requested is increasing the aircraft speed from 30 to 55 Kn in helicopter configuration.

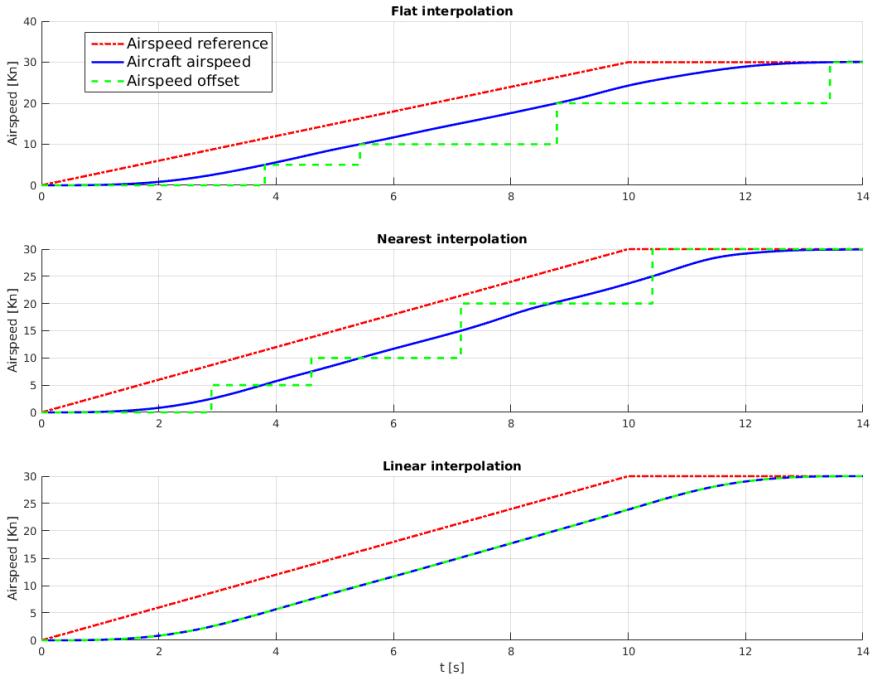

Figure 4.2: LPV interpolation methods

For regular grids of scheduling parameter values the default interpolation scheme is *linear* but for irregular grids only the *nearest* interpolation scheme is available.

The *linear* method provides the highest accuracy but takes longer to compute. The *flat* and *nearest* methods are good for models that have mode-switching dynamics but they are less accurate then the *linear* method. Their step interpolations of state-space models and offset easily trigger spurious leaps during simulations. In this thesis work this problem is even more present because control inputs are command derivatives.
It's then preferable to use a linear interpolation method but the LTI models grid available is of irregular type. This can easily be understood looking at figure 4.3. The XV-15 models array covers just the corridor envelope, therefore all the grid points external to the corridor have no state-space model and offsets associated. So the grid it's irregular.

To avail of the linear interpolation method and its better accuracy the irregular grid has been transformed to a regular grid through an artifice. Figure 4.4 represents

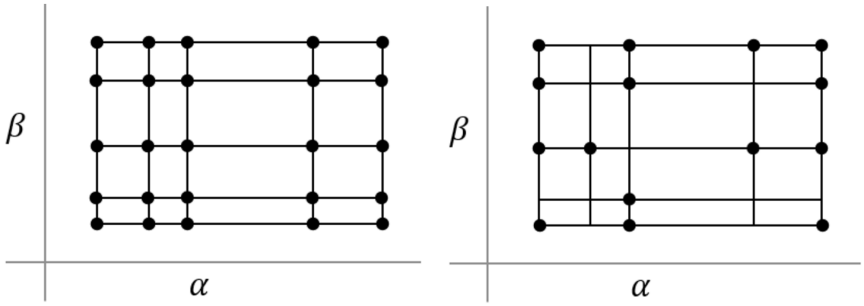

(a) Regular grid (b) Irregular grid

Figure 4.3: LPV grid types

this procedure: the grid points with no models associated (+) have been padded (◯) with the lowest or highest speed model for a given nacelles angle.

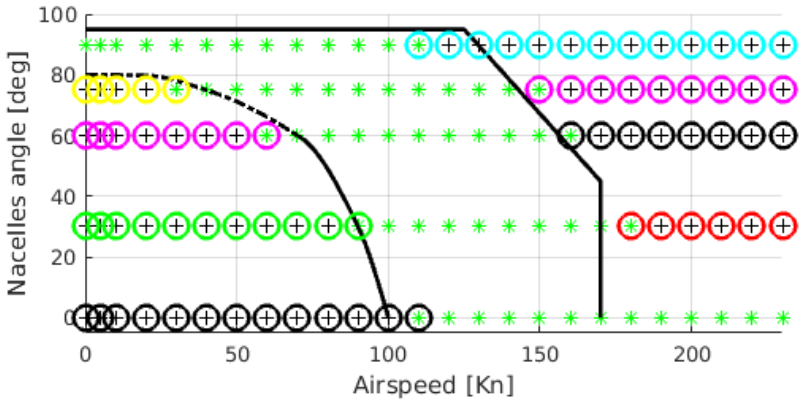

Figure 4.4: Padding to obtain a regular grid.
Each colored circle propragates the first or last model (∗) in the row.

Obviously this padding procedure to obtain a regular grid doesn't lead to a correct state-space interpolated model if simulation occurs outside the conversion corridor or close to its borders. Nevertheless the error simulating near to corridor borders is small and most simulations don't go close to the corridor boundaries. Said so, it's judge useful to avail of a linear interpolation.
Filling the grid with models in this manner can also be seen as choosing the *clip* extrapolation method within the LPV block. If selected, this extrapolation method disables extrapolation (makes a flat extrapolation) and returns the data corresponding to the last available scheduling grid point that is closest to the current point.

Chapter 5

Simulink implementation

5.1 Model description

The simulink model adopt the scheme reported in figure 3.2 with the main difference that the gain matrix K and the Sys_0 augmented plant block are here linearly interpolated in the parameter value $p(t)$: Starting from the left part of the scheme,

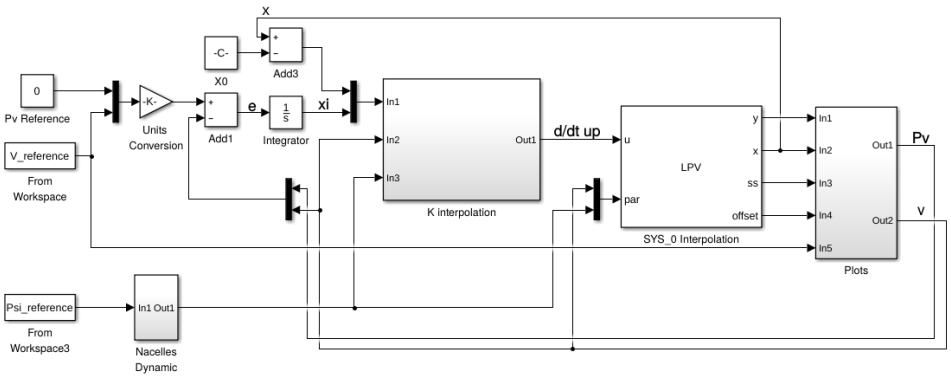

Figure 5.1: Simulink model

there are the vertical position P_v, the airspeed V and the nacelles angle ψ_n reference signals. The P_v reference is always set to zero because in this thesis work only conversion manoeuvres at a steady sea level altitude are studied. However the P_v reference can be used to simulate also climbs and descents of the tiltrotor.
After reference signals are fed they are subtracted by the actual P_v and V of the aircraft. This difference gives the two element error vector, which integrated becomes the x_i state vector.
x_i is the last part of the full-state vector χ. The first part of χ is composed by $x - x_0$, where x_0 contains all simulation initial state values excluding those of x_i which are null at simulation start.

The interpolated K matrix is switched in sign and multiplied by χ giving the commands derivative vector $\dot{u_p}$. This last is the input vector of the LPV block, which then outputs:

- y: the P_v and V linearized quantities
- x: all state vector excluded x_i
- SS: a state-space system which is the linear 2d interpolation of the state-space neighbours
- Offset: linear 2d interpolation of the offset vector neighbours.

The *Plots* block is organised to visualize all the quantities of interest. In particular the speed of the aircraft that is described in body axes through the states V_x and V_z is transformed in earth axes using simulink trigonometric non linear blocks. The results are defined as V_h and V_v and through integration of the last a non-linear reconstruction of P_v is made. Furthermore, a non-linear reconstruction of the aircraft airspeed is calculated as follows:

$$V = \sqrt{V_x^2 + V_z^2} \tag{5.1}$$

For a more accurate simulation these P_v and V non-linearly reconstructed quantities are then used as feedbacks and parameters instead of use the corresponding linearized quantities although the differences between non-linear and linear P_v and V remain contained in simulations. Figure 5.2 shows that the main differences are present in P_v reconstruction but they are contained within about seven feet.

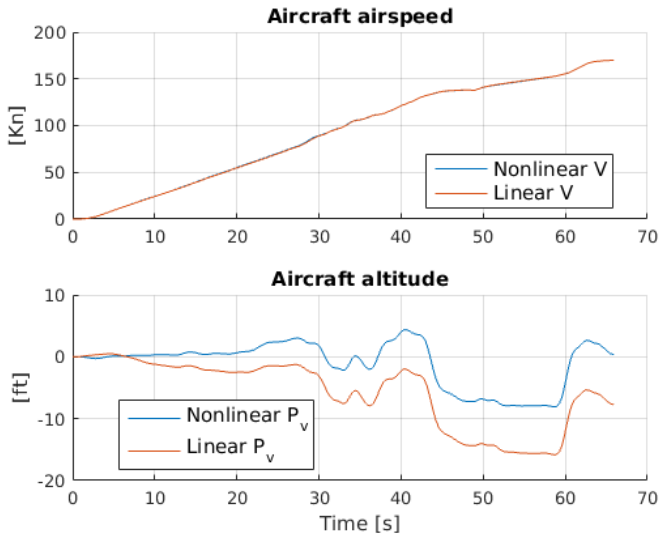

Figure 5.2: Nonlinear/linear airspeed and altitude reconstruction

As can be seen from figure 5.3 V has the double role of feedback and parameter variable.

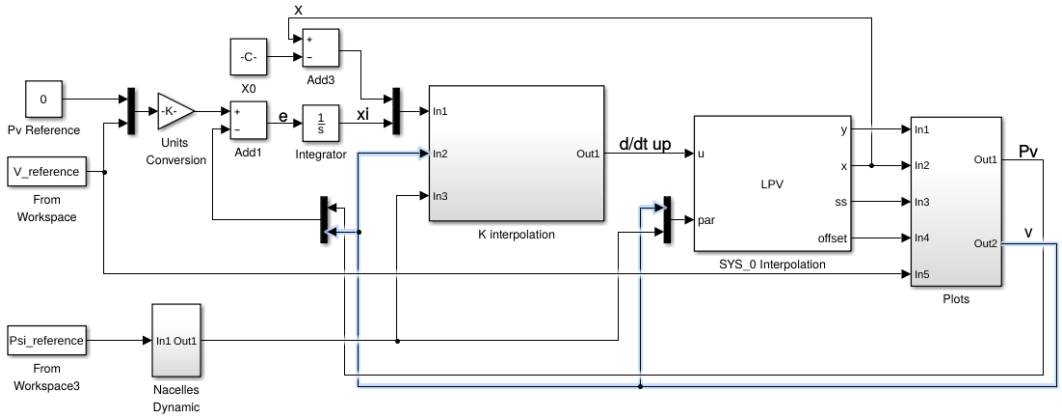

Figure 5.3: V feedback and parameter path

P_v is instead used only as feedback, as shown in figure 5.4.

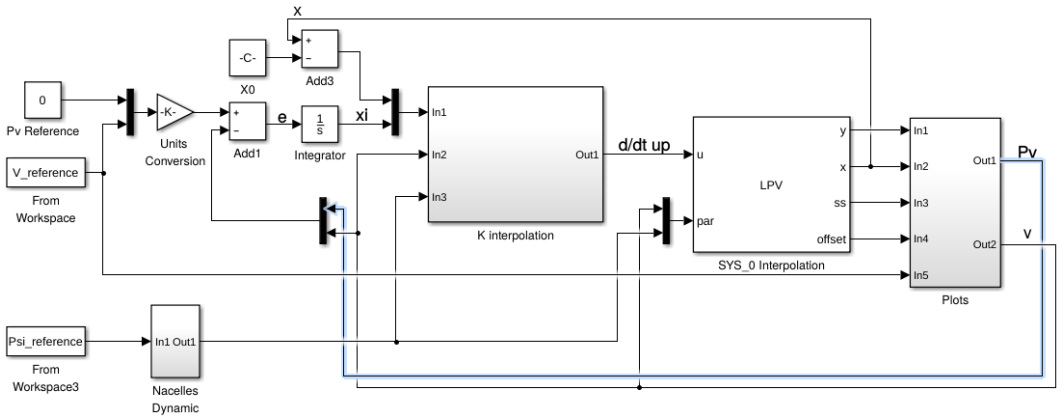

Figure 5.4: P_v feedback path

The second parameter passed at K and LPV blocks is $\psi_{n\ Ref}$ as can be seen in figure 5.5. The ψ_n reference goes through a *Nacelles Dynamic block* before reach K and LPV blocks. This block is basically constituted by the following second order transfer function:

$$G_N(s) = \frac{1}{(T_1 s + 1)(T_2 s + 1)} \tag{5.2}$$

where:

$T_1 = 0.3s$

$T_2 = 0.5s$

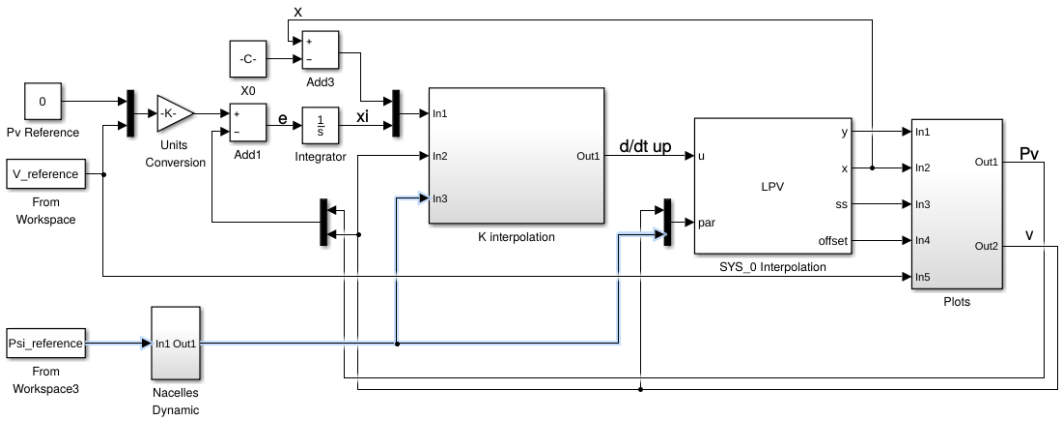

Figure 5.5: ψ_{ref} parameter path

The introduction of this dynamic allow to smooth the ψ_n reference, passing from a C^0 segmented curve to a C^1 curve as can be seen in figure 5.6. This imitate the true nacelles actuation dynamic which has a transitory due to nacelles inertia and limited actuation power. Anyway this modelling doesn't reproduce the exact nacelles dynamic for which sufficient data were not available.

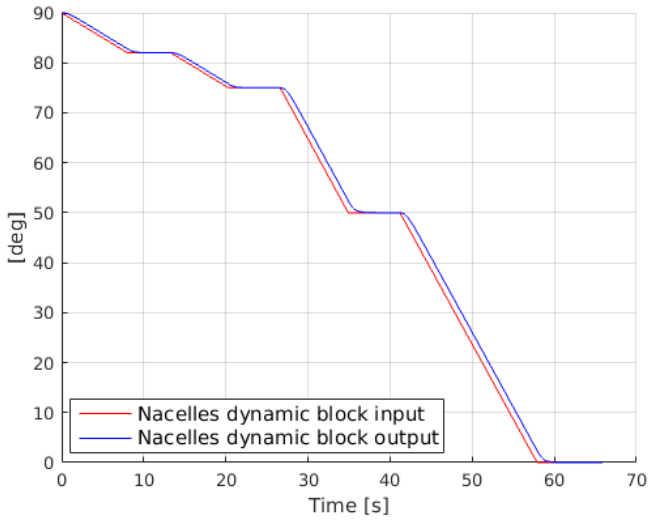

Figure 5.6: ψ_{ref} before and after the nacelles dynamic block

5.1.1 Gain matrixes interpolation

The gain matrix block differs from the LPV block principally because it doesn't comprehend offsets. As in the LPV block the interpolation is done trough the parameters $p(t)$, interpolating the 2d gain matrix K neighbours. Both interpolation and extrapolation are set to linear. Figure 5.7 presents the content of the *K interpolation block*.

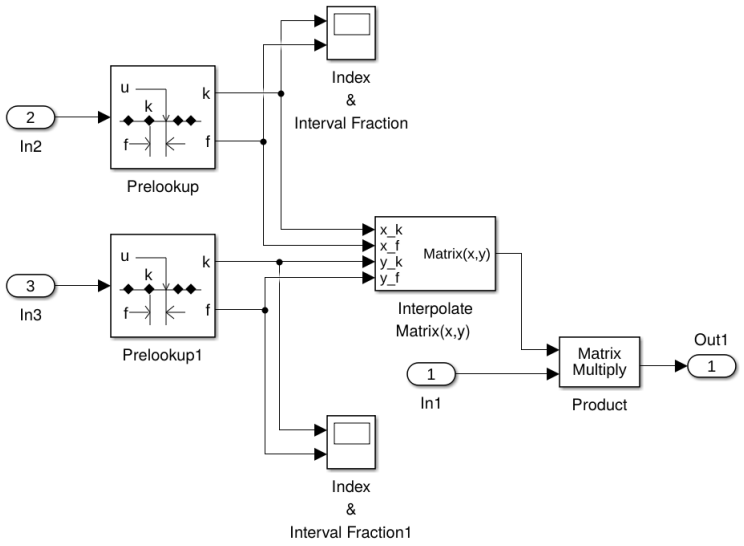

Figure 5.7: Gain matrix interpolation block subsystem

While in the LPV block the linear interpolation is automatically handled by the software, here it has been done using the *Prelookup tables* and the *Interpolate Matrix blocks* showed in figure 5.7. The *Interpolate Matrix* block is of the *kind Interpolation Using Prelookup block* and works always together with prelookup tables having these two blocks a distributed algorithm.
The prelookup table receives one parameter and outputs an index k and a fraction f. The index k represents the interval in which the parameter p(t) is situated in the p(t) linear grid while the fraction f represents the normalized position of p(t) inside the interval, ranging in values $0 \leq f < 1$. Feeding the resulting indexes and fractions values into the *Interpolate Matrix block* the 2d linear interpolation of the gain matrix K is obtained. The last operation done in the gain matrix subsystem is the multiplication between -K and the state vector χ (χ is represented by input 1). The subsystem then outputs $\dot{u}_p$ through output 1.

5.2 Full conversion results

A typical full conversion manoeuvre it's described in 6.2. The analysis that follows illustrates how the most significant states varies during this manoeuvre and when possible these quantities are compared with their offsets, that represent how the quantities should vary if the manoeuvre would take an infinite time.
The ψ_n values varies as described by the blue curve in figure 5.6 while the airspeed V has the trend reported in figure 5.8. The airspeed reference is chased quite well

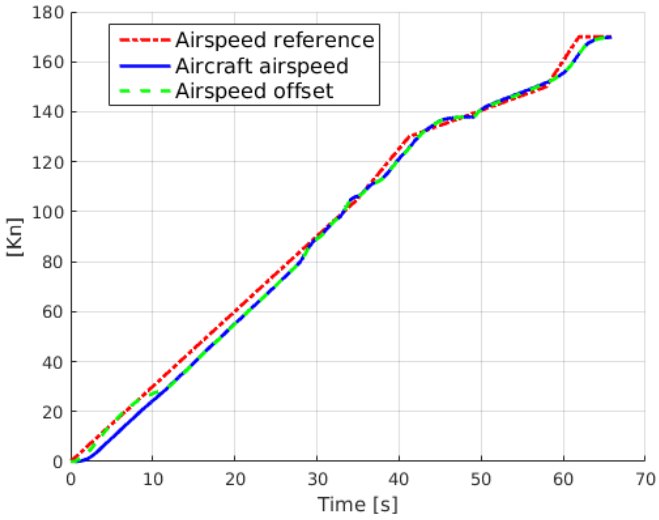

Figure 5.8: Airspeed V in the typical conversion manoeuvre

considering that the aircraft speed stays close to the reference during the whole conversion. The third dashed green curve is practically overlying the aircraft speed indicating that at each moment the V linear interpolation of the 2d neighbour offsets corresponds with the tiltrotor airspeed V.

Another important variable to track is P_v. Figure 5.9 reports it's trend.

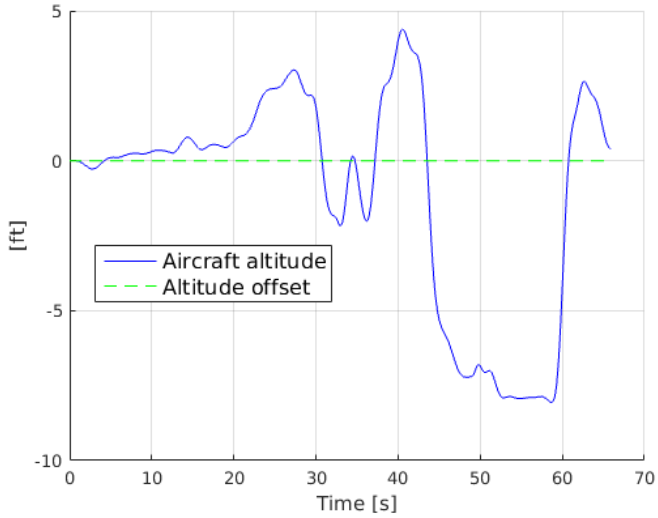

Figure 5.9: Vertical position P_v in the typical conversion manoeuvre

The dashed green curve represents the constantly null reference (and offset) while the blue curve represents the actual P_v course in the simulation. The maximum vertical position variation is of about 8 ft that can be regarded as a good altitude tracking.

The pitch state represent another important quantity describing the flight mechanics of the tiltrotor during conversion. Figure 5.10 reports θ course and its associated offset. It's interesting noting how the pitch value differs from offset especially in the first part of the simulation. This pronounced nose down situation at the beginning of the simulation it's needed to cope with the rapidly increasing V reference. With this negative pitch angle an additional horizontal thrust by rotors is obtained and the aircraft can gain speed even more quickly then with the only nacelles rotation.

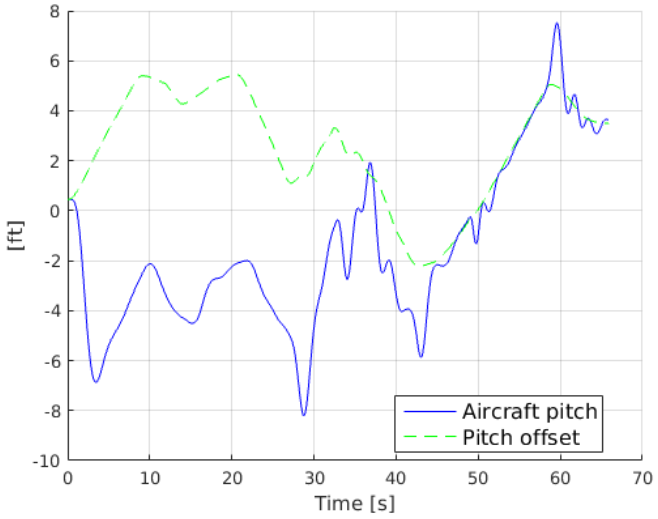

Figure 5.10: Pitch θ in the typical conversion manoeuvre

Chapter 6

Conversion optimization

6.1 Optimization goals

The conversion manoeuvre can be optimized on several aspects. The most interesting goals that can be considered are:

- Minimization of blades flapping
- Maximization of manoeuvre safety
- Simplification of pilot commands necessary to execute the manoeuvre
- Minimization of manoeuvre required time

The minimization of blades flapping is an interesting goal because it imply more than one advantage. If the medium blades flapping on a rotor revolution is contained the blades root stress will be contained too, without taking into account inertial loads due to elastic flapping modes. Furthermore, a contained blades flapping guarantee a safe tip blade - wing clearance and can also prolong the fatigue life of the rubber hub spring that realize the gimbal joint. Minimizing the cosine and sine gimbal states (X(4) and X(5)) is possible to minimize the medium blades flapping on a rotor revolution. With the scope of unify X(4) and X(5), the flapping minimization can be obtained through the single goal optimization with figure of merit:

$$X_g = \sqrt{X(4)^2 + X(5)^2} \tag{6.1}$$

Before optimize the conversion manoeuvre it's important to understand how this is executed today and how model states vary adopting this typical conversion path.

6.2 Typical conversion manoeuvre definition

Today AW-609 typical conversion manoeuvre starts with a hover at about 20 ft. In a helicopter the initial speed for a normal take-off is gained pushing forward the ciclyc stick while in the tiltrotor the pilot holds the nacelle switch forward for a few seconds resulting in a nacelles rotation from 90° to about 82°. So while in a helicopter the rotor thrust is tilted forward by the TPP forward tilting and by imposing a nose down attitude, in the tiltrotor the rotors thrust is tilted forward mainly by the nacelles tilting, maintaining a quite neutral attitude. It has to be noted that in this flight phase the pilot is asked to *hold* the conversion switch in order to tilt the nacelles so the pilot can select any angle between 90° and 75° simply realising the switch at the right moment. This nacelles control method it's valid from 90° to 75° and the nacelles tilt of one degree for each second the pilot holds the switch (1 deg/s nacelles tilting rate).
With this 82° slightly forward nacelles setting the tiltrotor accelerates reaching an airspeed of about 40 Kn. Keeping forward the nacelles switch again, nacelles rotates until the 75° where they automatically stops. This automatic stop prevents to get into the dangerous situation where nacelles are tilted to less than 75° but the aircraft is slow, close to the lower corridor boundary where stall can occur.
With nacelles still at 75° the aircraft reaches an airspeed of about 80 Kn and then the pilot gives a single input (without holding the switch) rotating the nacelles to 50° at a 3 deg/s nacelles rate. Maintaining this nacelles angle the aircraft reaches about 130 Kn. It's then time to complete the conversion giving another single input to the switch and bringing the nacelles in the 0° locked position, again at a 3 deg/s nacelles rate. At this point the aircraft has a speed of about 150 Kn and can accelerate and exit from conversion corridor at the speed of 170 Kn. When the tiltrotor is close to this speed the pilot gives a last input to the nacelles switch, lowering rotors RPM.
After each nacelles rotation there is a pause time in which the aircraft continue to increase its speed to reach the new desired velocity. These happens because typically the aircraft required time to accelerate from one desired speed to the next is bigger than the time required to tilt the nacelles. The typical conversion manoeuvre is therefore accomplished at steps as can be seen in figure 6.1. The red dash-dot line represents the simulation reference while the red thick continuous line represents the corridor path that the pilot has been able to achieve. The dashed black line represents the conversion corridor center.

The tracking signals necessary to create the reference reported in figure 6.1 are reported along with the time vector in table 6.1. This vector is determined by the nacelles rotational speed and by the aircraft acceleration capacity at different speeds,

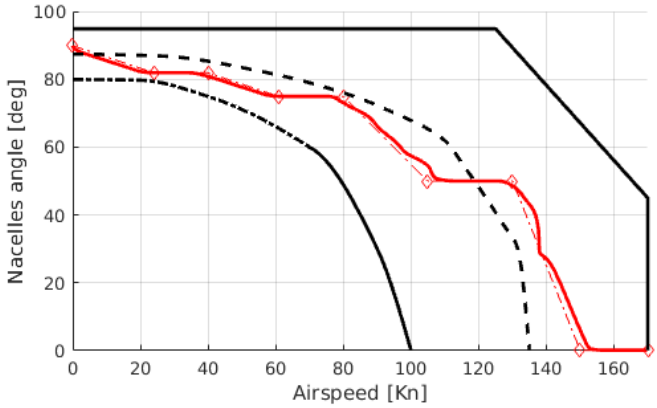

Figure 6.1: Typical conversion manoeuvre path

which have been reconstructed to be those reported in table 6.2. Only in the last two column passage (table 6.1) the time vector does not depend on this two variables: in fact at the end of each simulation four seconds has been added to allow the aircraft to reach the desired end speed of 170 kn.

V_{Ref}	0	24	40	61	80	104.9	130	150	170	170
ψ_n	90	82	82	75	75	50	50	0	0	0
t	0	8	13.3	20.3	26.6	34.9	41.2	57.9	61.9	65.9

Table 6.1: Tracking signals

ψ_n range [deg]	90-90	90-75	75-50	50-0	0-0
Nacelles rate [deg/s]	/	1	3	3	/
Aircraft typical acceleration [Kn/s]	3	3	3	4	5

Table 6.2: Nacelles rate and aircraft acceleration in function of ψ_n

Therefore at simulation start going from $\psi_n = 90°$ to $\psi_n = 82°$ requires 8 seconds due to nacelles rotational speed. Immediately after, maintaining the nacelles at $\psi_n = 82°$ and considering a typical aircraft acceleration of 3 Kn/s, a time of 5.3 seconds is required to increase the airspeed from 24 to 40 Kn. This time summed to the initial 8 seconds gives the 13.3 seconds result in the third column of table 6.1. Iterating this calculations is possible to recover all values in table 6.1.

6.3 Rotor flapping

During the typical conversion manoeuvre just defined the flapping quantity X_g defined in eq. 6.1 assumes the values reported in figure 6.2. In the graph legend are reported the maximum X_g value, the conversion time t_c that measure the time in which the aircraft reaches the airplane configuration and the final simulation time t_f in which the aircraft attains the final required speed of 170 Kn. The value $X_g(t_c)$ is marked with a circle.
The other most important states vary as in figure 6.3.

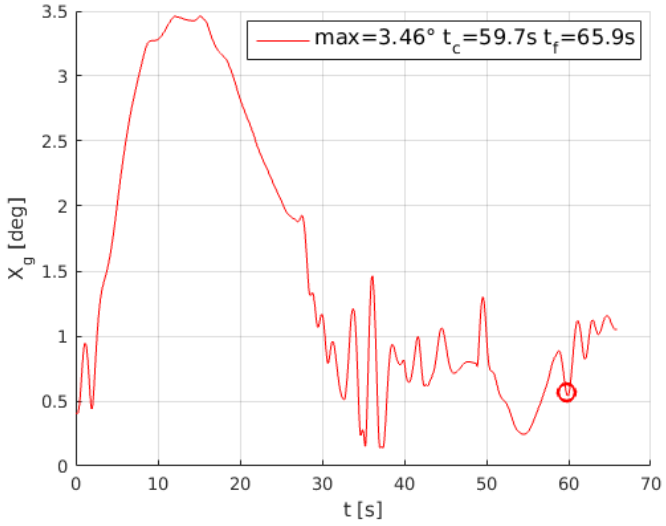

Figure 6.2: X_g during a typical conversion manoeuvre

As can be seen in figure 6.2 X_g has a peak in the first part of the conversion manoeuvre. This is due to the high value of $|X(5)|$ (| | indicates the absolute value) offset at nacelles angles near to vertical and at low speed. Offset values has to be regarded as the value that would occur if the manoeuvre is executed in an infinite time. So X_g simulation values do not correspond to X_g offset values because of the manoeuvre dynamics. From the 3D offset graph of $|X(5)|$ reported in figure 6.5(b) the peak just cited is of immediate visualization. The offset trend of $|X(4)|$ is reported in figure 6.4.

X_g offset values can be calculated as:

$$X_{g_{Off}} = \sqrt{X(4)^2_{Off} + X(5)^2_{Off}} \tag{6.2}$$

The trend of X_g offset is reported in figure 6.6.

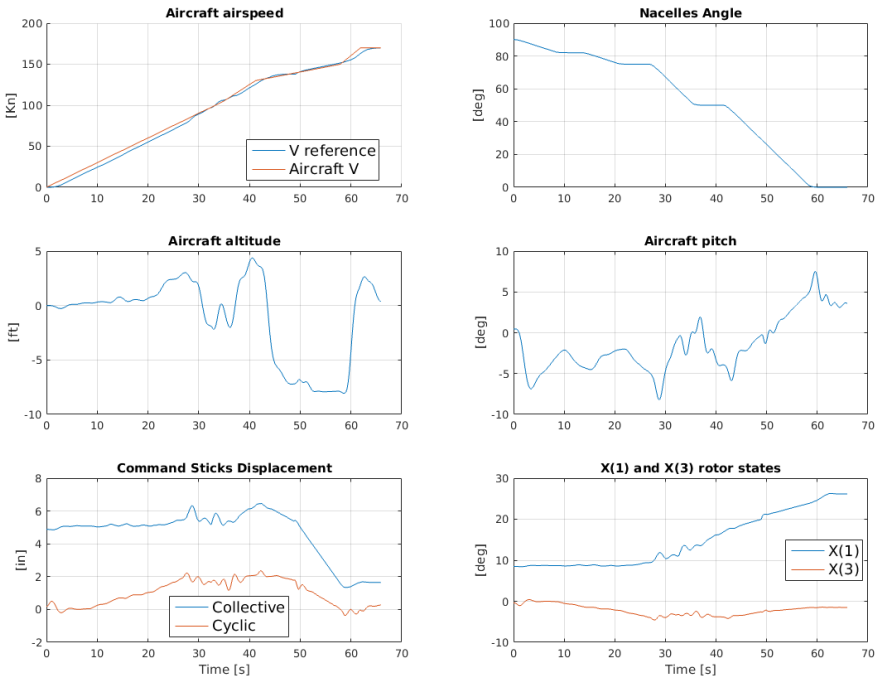

Figure 6.3: Most significant state trends during a typical conversion manoeuvre

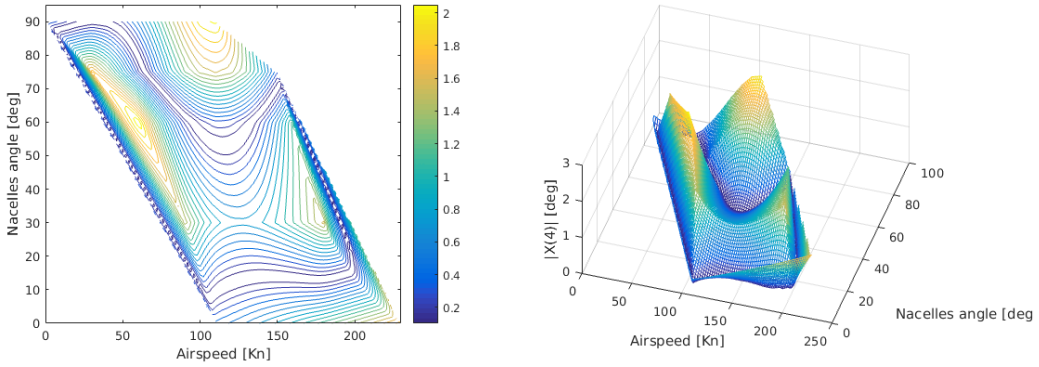

(a) $|X(4)|$ offset 2D graph

(b) $|X(4)|$ offset 3D graph

Figure 6.4: $|X(4)|$ offsets on corridor domain

A possible way to minimize X_g could be following the minimum X_g offset values path. This path can easily be spotted on X_g 3D figure 6.6(b) and is reported in figure 6.7. However the results are disappointing as can be seen in figure 6.8. In fact, following this minimum X_g offset path the first part of the simulation reveals that

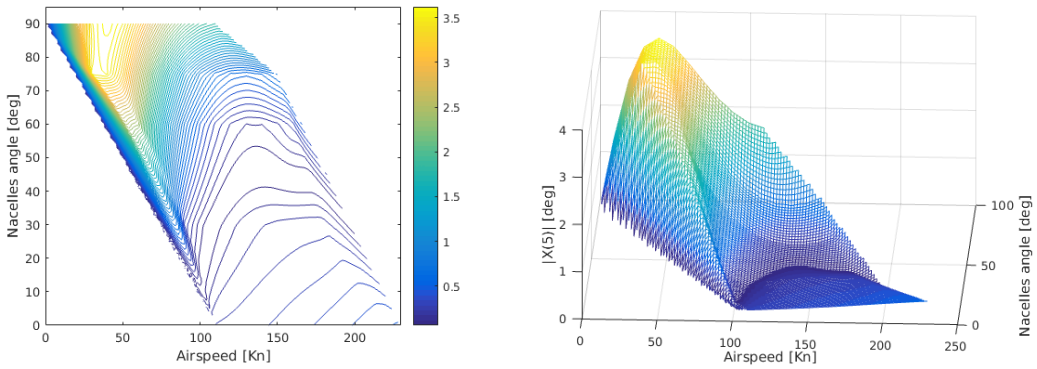

(a) $|X(5)|$ offset 2D graph (b) $|X(5)|$ offset 3D graph

Figure 6.5: $|X(5)|$ offsets on corridor domain

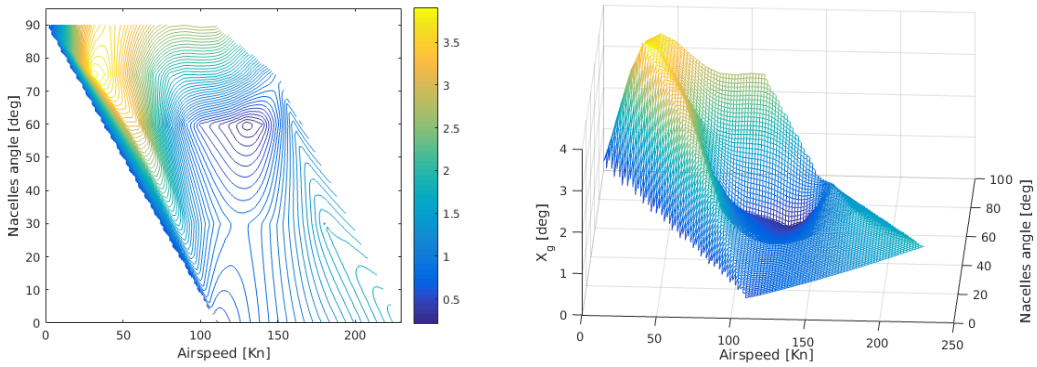

(a) X_g offset 2D graph (b) X_g offset 3D graph

Figure 6.6: X_g offset on corridor domain

X_g has an higher value than in the typical conversion manoeuvre exposed before. This is due to the dynamics involved that rise the X_g values with respect to their offset values. Also the time required to perform the conversion becomes a lot longer.

The conversion can also be done with higher nacelles rotational speed. In the angle range from 75° to 0° the rotational speed can be selected to be 3 deg/s or 8 deg/s to speed up the conversion. A conversion manoeuvre similar to the typical conversion manoeuvre as corridor path but that adopts the 8 deg/s nacelles rate is shown in figure 6.9. The X_g graph in this fast conversion presents evident oscillations and high X_g values as can be seen in figure 6.11. In fact, the higher nacelles rate imply a quick modification of the tiltrotor configuration forcing the pilot to act faster and more abruptly on commands to keep the aircraft at a level attitude and at a steady altitude while the aircraft accelerates. Figure 6.10 shows this wide and fast action

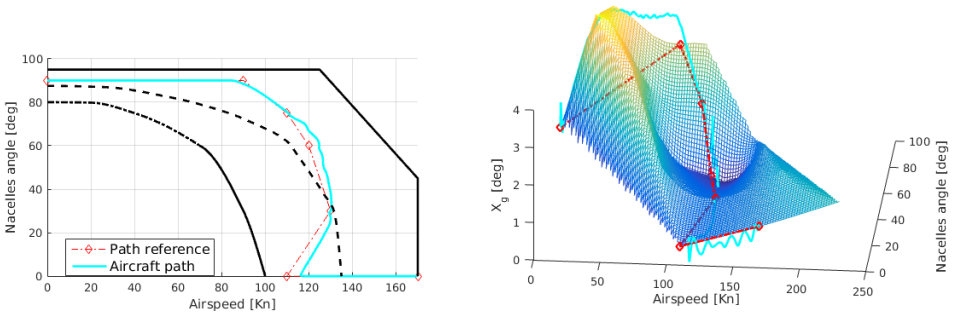

(a) 2D path (b) 3D path

Figure 6.7: Minimum X_g path on conversion corridor

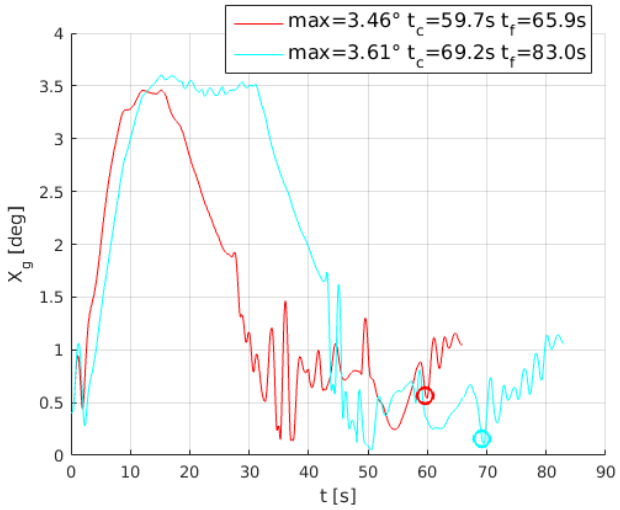

Figure 6.8: X_g trend following the min X_g offset path

on controls. This more powerful commanding amplifies X_g oscillations leading to the results shown in figure 6.11. So a strict correlation exists between nacelles rate and X_g oscillations: the more the rate the higher the X_g peak values.

Therefore a good strategy for minimizing X_g can be choose a low nacelles rotation rate, as 2 deg/s. Also slowing down the nacelles rotational speed permits to execute the conversion without having to pause after a nacelles rotation waiting for the aircraft to reach an higher speed, adequate for a further nacelle tilting. The resulting conversion corridor path is no more at steps but a quite straight curve as that reported in figure 6.12. X_g trend with this 2 deg/s nacelles tilting rate is reported in figure 6.13. As can be seen oscillations are reduced but initial high X_g values

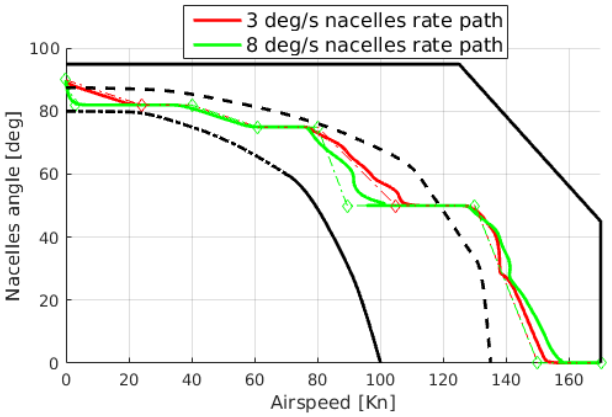

Figure 6.9: 8 deg/s nacelles rate conversion path

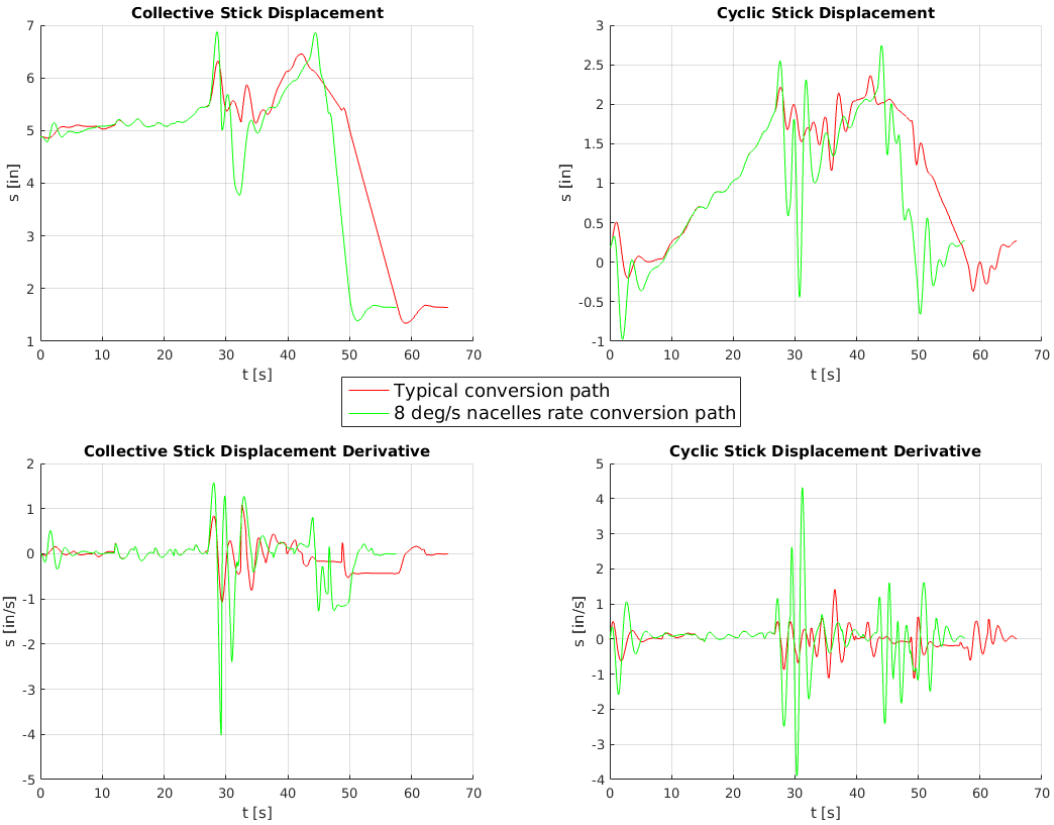

Figure 6.10: 8 deg/s nacelles rate conversion command histories

remain.

It would exist a particular path that can reduce this X_g initial peak, so an optimization is implemented to explore several path possibilities and find the best

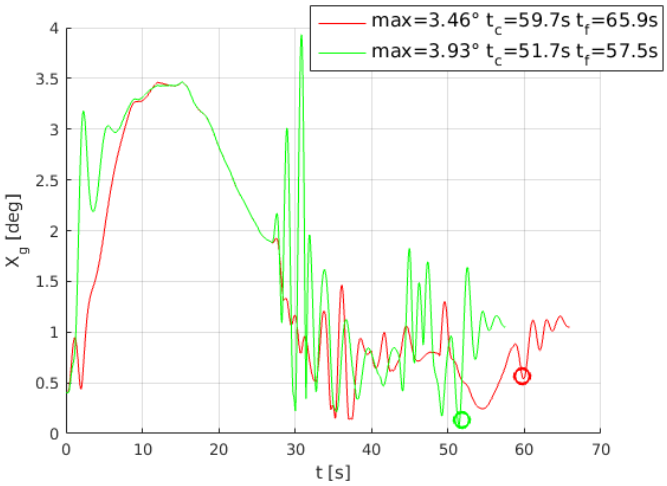

Figure 6.11: 8 deg/s nacelles rate X_g trend

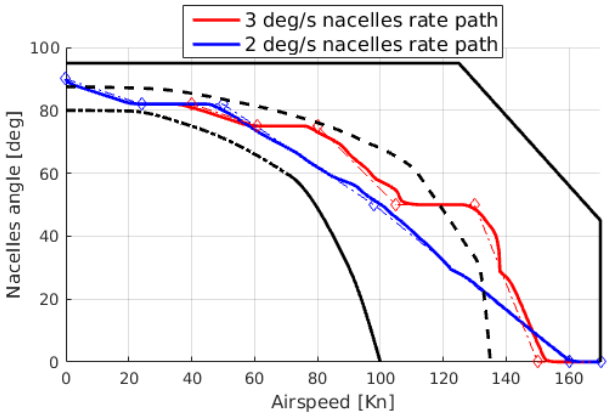

Figure 6.12: 2 deg/s nacelles rate conversion path

one. At this scope the *GA Matlab Genetic Algorithm* is used, imposing a 1 deg/s nacelles rate from 90° to 75° and a 3 deg/s rate from 75° to 0°. The optimizer figure of merit is:

$$F = min\left(\frac{1}{T_f}\int_0^{T_f} X_g(t)\,\mathrm{d}t\right) \tag{6.3}$$

Instead of minimizing the maximum X_g value it has been preferred to minimize the area underneath the X_g curve because the X_g maximum value at the end of the optimization was going to be one of the high values at the beginning of the simulation preventing then to find a path that also minimize X_g after this first conversion part. Also, the division by the final simulation time T_f allow to have a figure of merit that is less dependent on the conversion required time.

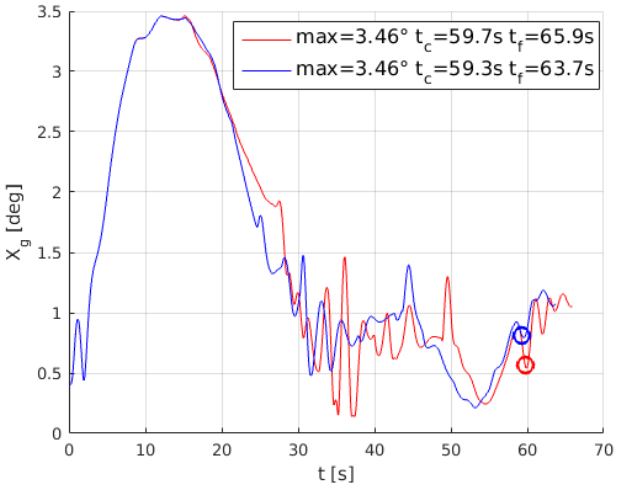

Figure 6.13: 2 deg/s nacelles rate X_g trend

The optimization boundaries are composed by lower and upper speed limits at different ψ_n. The boundary values are reported in table 6.3 and they are represented with thick red lines in figure 6.14. The set of linear inequalities 6.4 completes the optimization constrains set forcing the optimizer to find a conversion path in which the airspeed monotonically increases while the nacelles angle decreases.

ψ_n	Lower boundaries	Upper boundaries
90	0	110
82	0	120
75	62	130
50	87	153

Table 6.3: Lower and upper speed boundaries

$$\begin{bmatrix} 1 & -1 & 0 & 0 \\ 0 & 1 & -1 & 0 \\ 0 & 0 & 1 & -1 \end{bmatrix} \begin{Bmatrix} V_{\psi_n=90^\circ} \\ V_{\psi_n=82^\circ} \\ V_{\psi_n=75^\circ} \\ V_{\psi_n=50^\circ} \end{Bmatrix} \leq \begin{Bmatrix} -24 \\ -21 \\ -25 \end{Bmatrix} \tag{6.4}$$

Considering the first inequality:

$$V_{\psi_n=82^\circ} - V_{\psi_n=90^\circ} \geq 24$$

The known term derive from the fact that a nacelles rate of 1 deg/s and an aircraft acceleration of 3 Kn/s have been considered in the first conversion part.

Tilting the nacelles from $\psi_n = 90°$ to $\psi_n = 82°$ with such rotational speed requires 8 seconds, that multiplied by the aircraft acceleration gives 24 Kn gained speed. With similar consideration is possible to calculate the other known terms in 6.4.
The optimizer tries span almost all the conversion corridor as can be seen in figure 6.14 and the optimal conversion path returned is that reported in figure 6.15. The X_g trend for this optimal path is represented in figure 6.16. As can be seen from

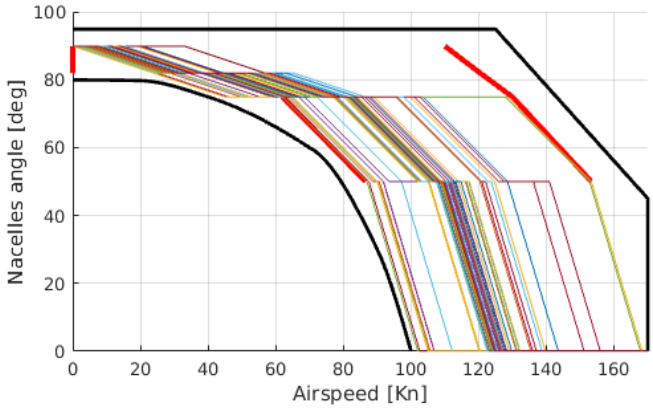

Figure 6.14: Optimizer path tries

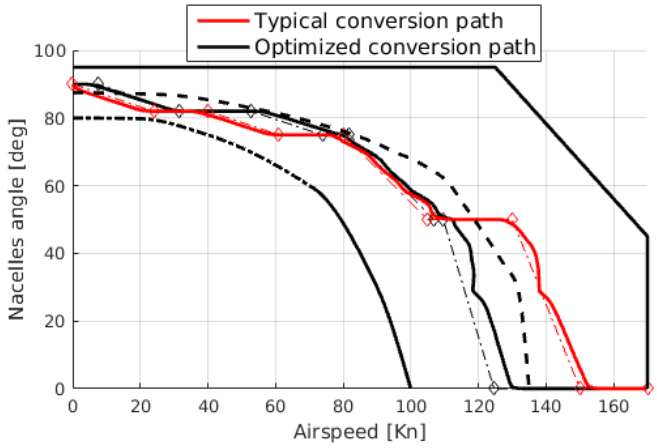

Figure 6.15: Optimizer path choice

figure 6.15 the optimizer finds a conversion path similar to the typical conversion manoeuvre and with similar X_g results. In fact X_g oscillations are present in the same amount as in the typical conversion manoeuvre, indicating a similar pilot control effort for both conversion paths. Most important, the maximum X_g value is the same, indicating there's no optimal path that can avoid this initial high X_g

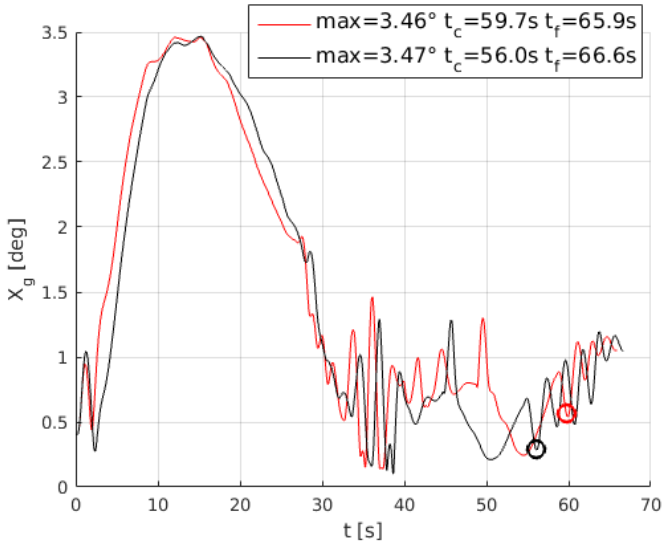

Figure 6.16: X_g trend for the optimized path

value.
This optimization limitation can be understood looking at the X_g offset trend. In the initial phase of the conversion the manoeuvre is sufficiently slow to have a X_g trend very close to the X_g offset trend, as shown in picture 6.17. Therefore X_g values can eventually be lower of X_g offset values but only for a small amount.

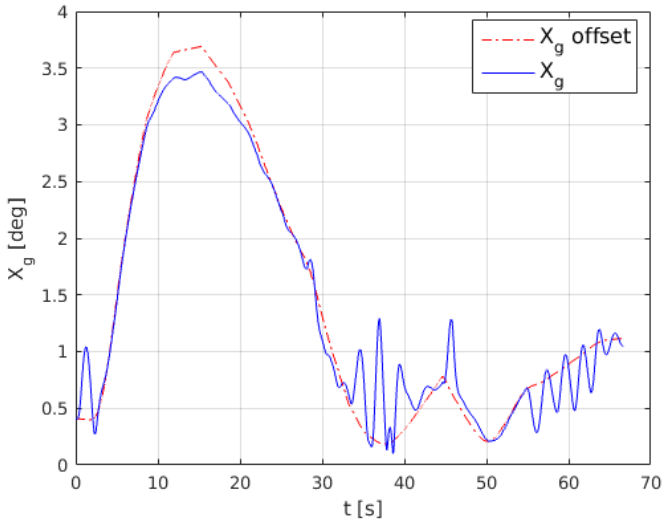

Figure 6.17: X_g offset and X_g trends

6.4 Manoeuvre safety

The conversion manoeuvre safety is maximized when the aircraft conversion path coincides with the middle of the conversion corridor. In fact this guarantee the maximum safety margin from stall and from high speed boundaries.

Figure 6.18 shows a conversion path very close to the middle of the corridor. In this conversion the nacelles are tilted at steps with a rate of 3 deg/s and the pilot has to pay attention to regulate the aircraft speed to stay in the corridor center. This is not an easy task because of the different aircraft accelerations required in the different conversion phases. Figure 6.19 reports the required aircraft acceleration to stay in the middle of the corridor.

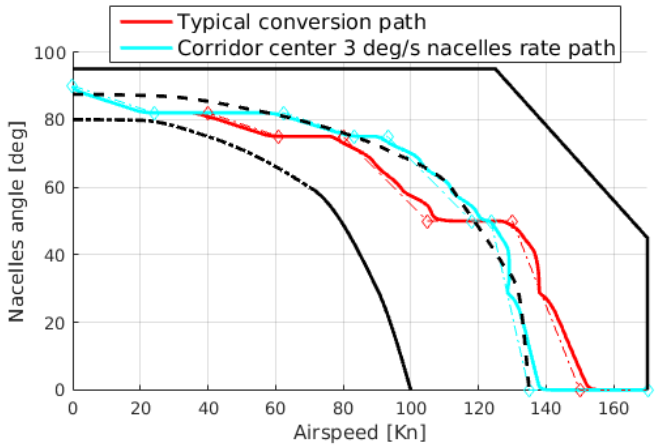

Figure 6.18: Center corridor conversion path with 3 deg/s nacelles rate

The pilot control effort to execute the manoeuvre is comparable with that necessary to execute the typical conversion manoeuvre as can be seen from command and command derivative histories in figure 6.20.

The manoeuvre just exposed effectively maximizes the conversion safety maintaining the aircraft in the middle of the corridor. A moderate pilot control effort is necessary for stabilizing and tracking the aircraft speed as in the typical conversion case. A more penalizing factor is the time required to accomplish the conversion, that reaches 60.2 seconds. The medium flapping X_g has the same maximum value as for the typical conversion and also oscillations are similar to that in the typical conversion case. X_g trend is reported in figure 6.21.

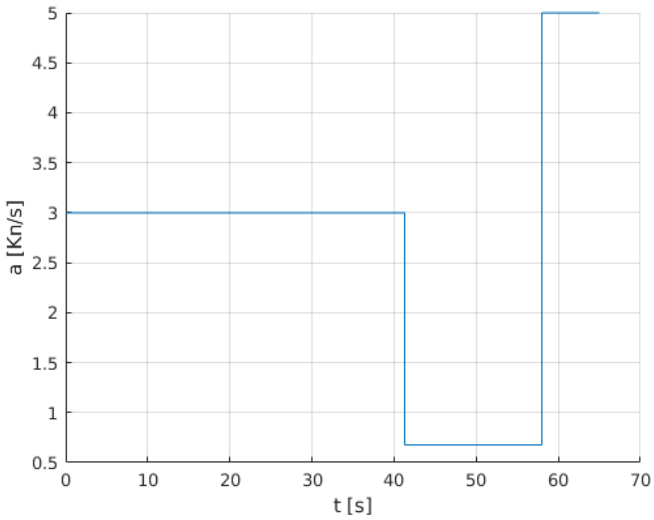

Figure 6.19: Required aircraft acceleration profile

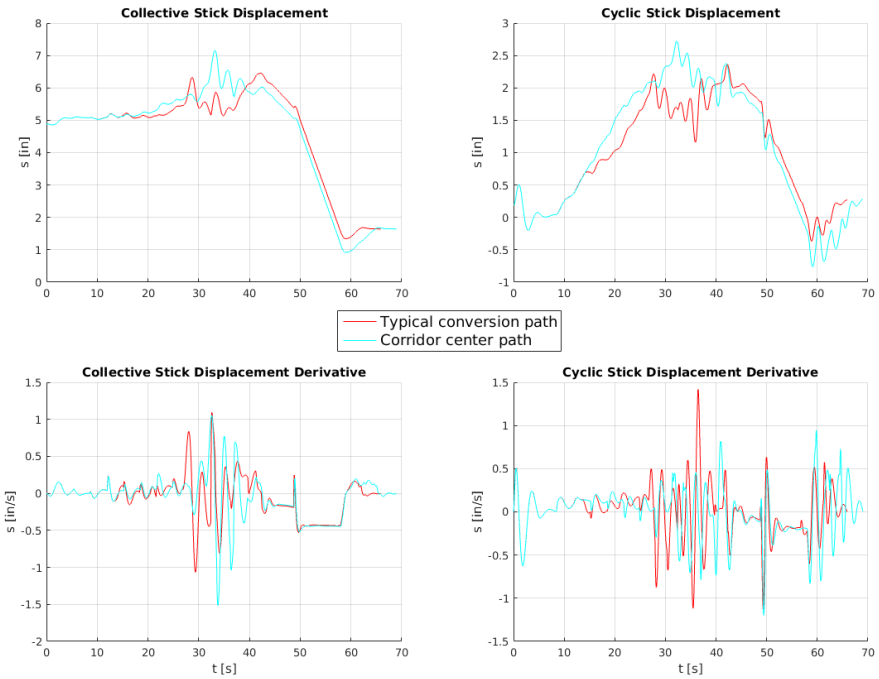

Figure 6.20: Corridor center command histories

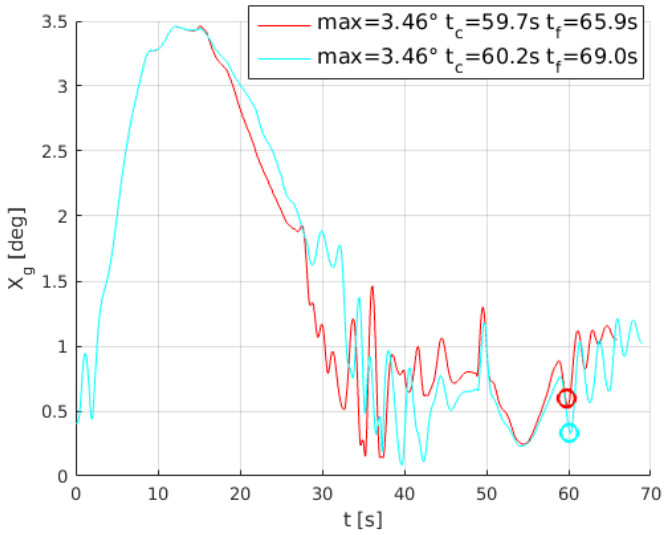

Figure 6.21: Corridor center X_g trend

Another possible choice to execute the conversion manoeuvre staying as close as possible to the corridor center is to select a certain aircraft acceleration story as that reported in table 6.2 and adjust the nacelles angle as the aircraft gains speed. This would be possible with an automatic control of nacelles angle with the aircraft speed. This automatic nacelles control would act from 82° to 0° on pilot request.

The new conversion pilot procedure would occur as:

- hold the conversion switch to bring the nacelles from 90° to 82°
- reach a speed of about 60 Kn that corresponds to the corridor center at this nacelles angle
- engaging the automatic nacelles control tilting further the nacelles holding the switch for a couple of seconds
- keep a level attitude while the nacelles tilt conformally to airspeed, mantaining automatically the aircraft in the corridor center
- once reached the airplane configuration, another input to the switch lowers the rotor RPM.

This conversion method have three basic advantages:

1. Less pilot work required. The nacelles are automatically tilted in function of the aircraft speed eliminating the pilot task to keep the aircraft within the conversion corridor. Also the pilot has no more to use the switch at 75° and at 50° nacelles angles.

2. It is a safer conversion manoeuvre because there is no possible pilot error in maintaining the aircraft within the corridor. Furthermore the aircraft stays on the corridor center during the manoeuvre.
3. A faster conversion is possible. The aircraft acceleration profile is more omogeneus. The aircarft continually accelerates reaching the airplane configuration in less time compared to the case with a fixed nacelles rate of 3 deg/s.

This nacelles control strategy imply a rotating nacelles speed that varies at steps along the conversion. Figure 6.22 report the aircraft corridor path using this proposed conversion scheme. The nacelles rate steps are reported in figure 6.23. As can

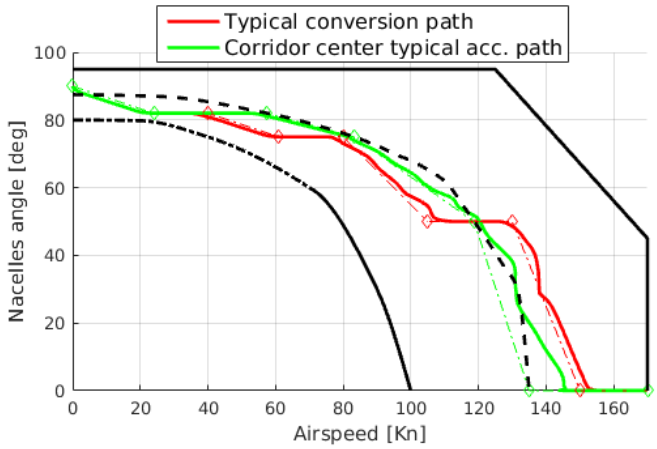

Figure 6.22: Center corridor conversion path with typical acceleration profile

be seen in figure 6.23, in the last conversion part nacelles rotational speed assumes a high value as 12.3 deg/s. This high nacelles rate is required to keep the aircraft in the middle of the conversion corridor. In fact, from 50° to 0° nacelles angle is assumed that the aircraft accelerates at 4 Kn/s and the aircraft speed at $\psi_n = 50°$ is close to the speed at $\psi_n = 0°$. So, in just about 4 seconds the nacelles have to tilt of 50 degrees implying a nacelles rate of about 12.3 deg/s. This also imply a very quick change in the aircraft configuration and then a fast commanding action by the pilot to keep the aircraft trimmed. Looking at picture 6.24 is possible to see an increased pilot action in this last conversion phase. At this high nacelles rate in the last part of the conversion corresponds also high X_g oscillations, as shown in figure 6.25. To overcome this fast nacelles rate problem one can reduce the aircraft acceleration in the last part of the conversion but this would cause to increase the total time required by the manoeuvre and the effort by the pilot to retain the aircraft acceleration.

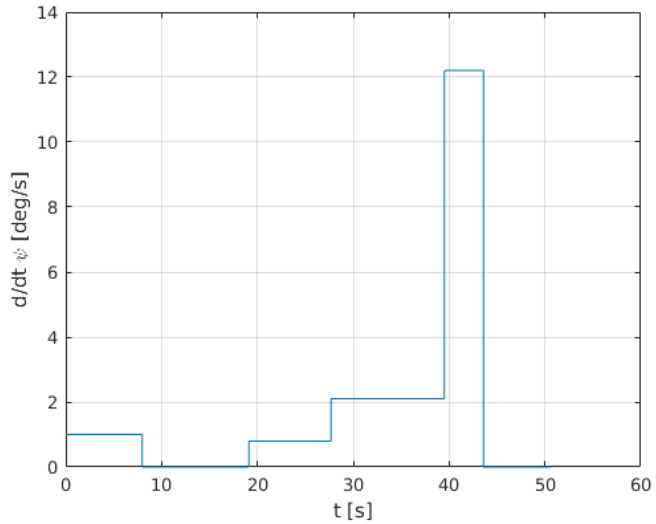

Figure 6.23: Nacelles rotational speed

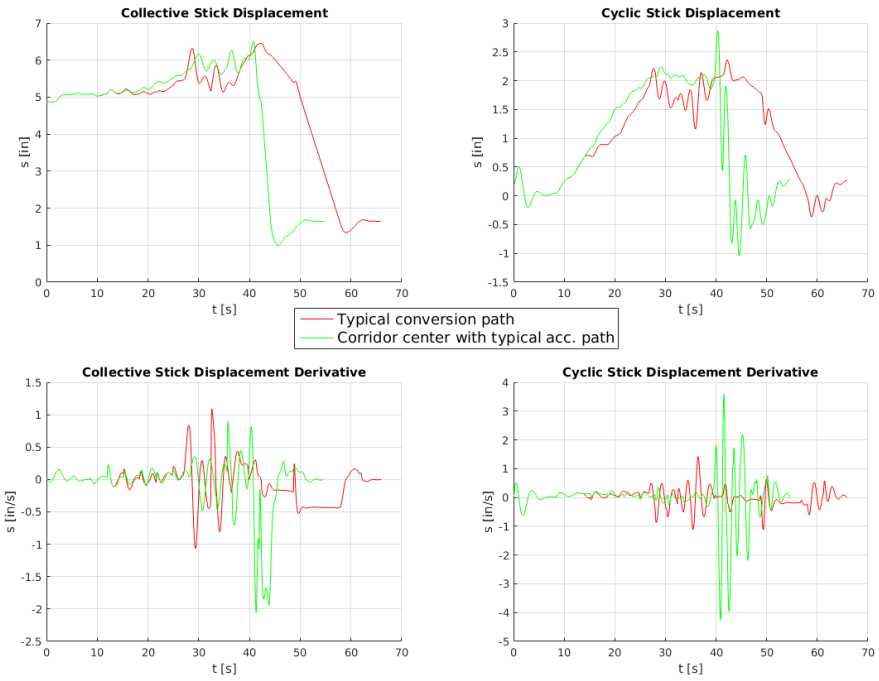

Figure 6.24: Center corridor with typical acceleration command histories

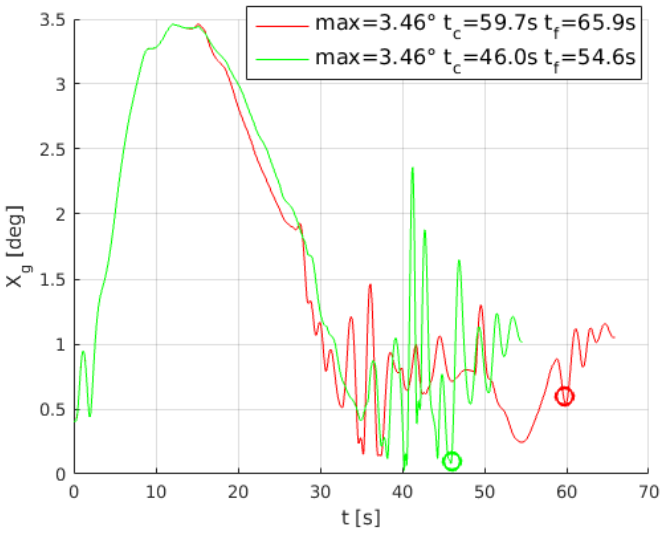

Figure 6.25: Center corridor with typical acceleration X_g trend

However it is going to be shown in 6.5 that slightly modifying the conversion path remaining anyway close to the middle of the corridor is possible to maintain a typical acceleration profile and at the same time obtain a more homogeneous nacelles rate.

6.4.1 Near stall manoeuvre

It appears to exist a certain pilots tendency to execute the manoeuvre staying close to the conversion corridor left boundary which represents the stall limit. This conversion path is reproduced in figure 6.26.

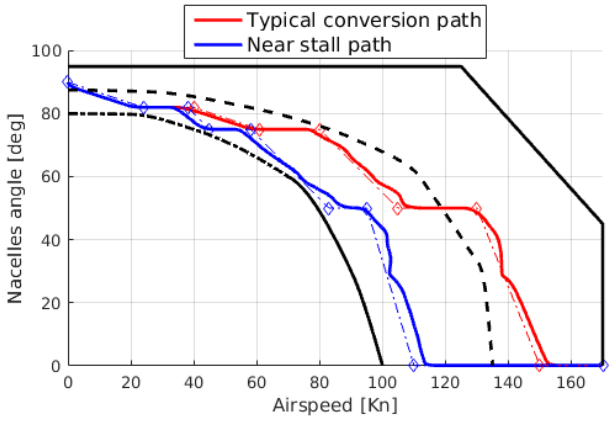

Figure 6.26: Near stall conversion path

The commands imparted by the pilot to execute the manoeuvre are reported in 6.27 while the X_g trend is reported in figure 6.28.

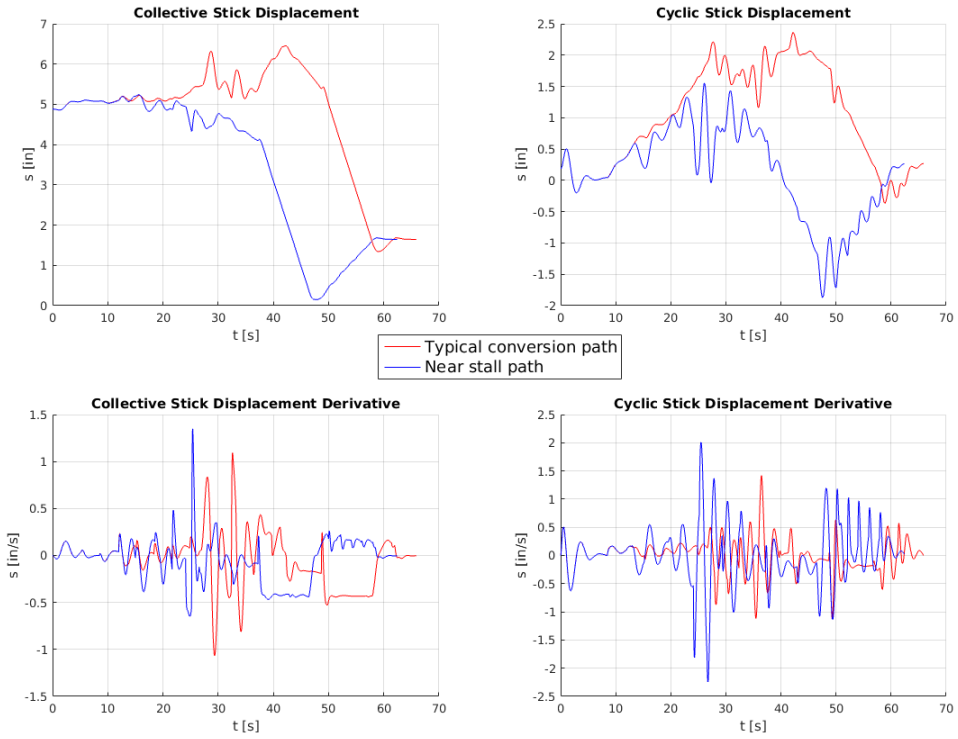

Figure 6.27: Near stall conversion command histories

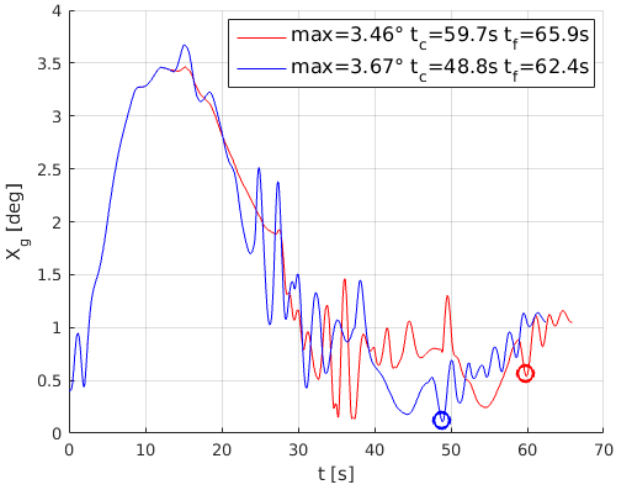

Figure 6.28: Near stall conversion X_g trend

Looking at figures 6.26 and 6.27 it seems there is no reason why pilots are induced to follow this conversion path. In fact, during almost all the manoeuvre the safety margin is very limited and a particularly dangerous situation happens when the aircraft reaches the 50° nacelles angle, where the wing is producing a large part of the lift but the aircraft is very close to the stall limit. Also looking at the command histories is possible to see how the lower aircraft longitudinal stability due to low airspeed implies a more powerful commanding with respect to the standard manoeuvre, especially for the cyclic control.
One reason to choose this near stall conversion could be the less time required to complete the conversion. Figure 6.28 shows that the time required to accomplish this manoeuvre is of only 48.8 seconds while the typical conversion manoeuvre requires 59.7 seconds. Along with this reduced time to complete the conversion, pilots could be induced to the near stall manoeuvre because of the less power required.
Anyway, these reasons do not justify the poor safety of the manoeuvre, which should be avoided.

6.5 Improved conversion manoeuvre

Slightly modifying the conversion path of the second manoeuvre exposed in 6.4 is possible to achieve a conversion manoeuvre that have several advantages albeit making some compromises.

To slow down the nacelles rotational speed maintaining the desired aircraft acceleration of 4 Kn/s in the last part of the conversion it's required to distance the reference speed at 50° and at 0° nacelles angles. The more this two reference speeds differs the more time is available to tilt the nacelles of the last 50 degrees, allowing for a lower nacelles rate.
A logical conclusion is to define a new *airspeed - nacelles angle relation* in which the reference speed at $\psi_n = 50°$ is less than the center corridor speed at this nacelles angle while the reference speed at $\psi_n = 0°$ is more than that indicated by the center corridor at 0° nacelles angle. In other words, the aircraft conversion corridor path is less vertical and intersect the corridor center line going from the upper left to the lower right in this last conversion phase. This new reference path is reported in figure 6.29.

It is clear from figure 6.29 that this new reference imply a compromise for the manoeuvre safety. In fact the aircraft is no more exactly in the middle of the corridor but it stays within a speed band about the center. Considering that the nacelles angle is automatically controlled this approach decreases manoeuvre safety

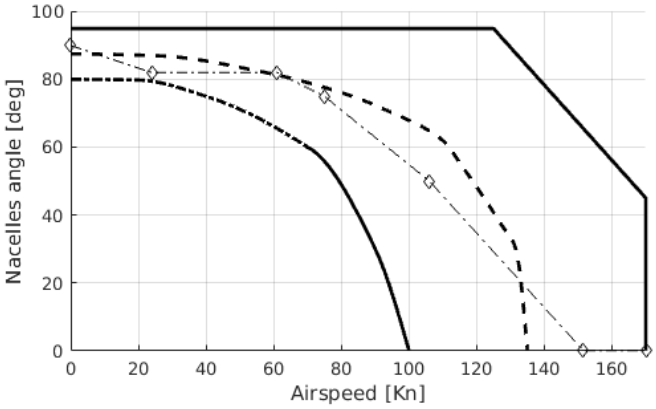

Figure 6.29: Improved conversion reference path

very little. The aircraft is in fact closer to the corridor boundaries but the nacelles automatic control will ensure that the aircraft stays within the corridor.
The reference curve in figure 6.29 has been determined again by the GA Matlab optimizer. The optimizer has been set to minimize control derivatives in order to minimize the pilot control effort during the manoeuvre. Therefore the optimizer figure of merit is:

$$F = min\left(\frac{1}{T_f}\int_0^{T_f} |\dot{u}_{COLL}(t)| + |\dot{u}_{CYCL}(t)|\,\mathrm{d}t\right) \tag{6.5}$$

The optimization boundaries are defined as in table 6.4. The boundaries are designed to force the optimizer to find a path that effectively minimize control derivatives but at the same time stays close enough to the corridor center.

ψ_n	Lower boundaries	Corridor center	Upper boundaries
82	57.4-15	57.4	57.4+10
75	83.2-10	83.2	83.2+15
50	118.7-15	118.7	118.7+5
0	135-5	135	135+15

Table 6.4: Optimization boundaries about corridor center

The optimization boundaries define then a band that is around the corridor center. This band is more tight where the corridor is narrower so the width of the band is not uniform. Also the band has been designed to guarantee an increasing speed path while the nacelles angle decreases. Figure 6.30 shows the band borders in thick red lines and the optimizer tries to find the optimal reference.

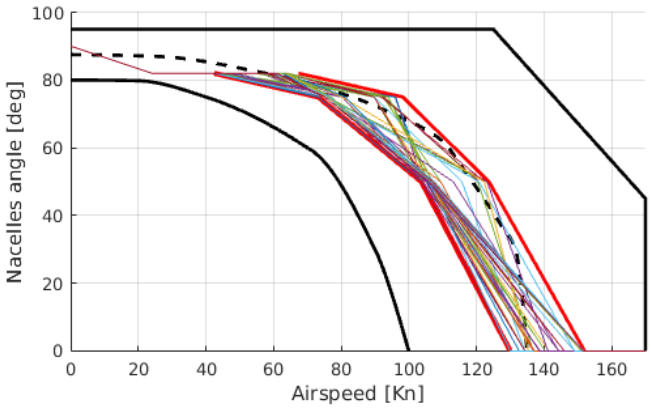

Figure 6.30: Optimizer tries

The improved conversion path returned by the optimizer is reported in figure 6.31.

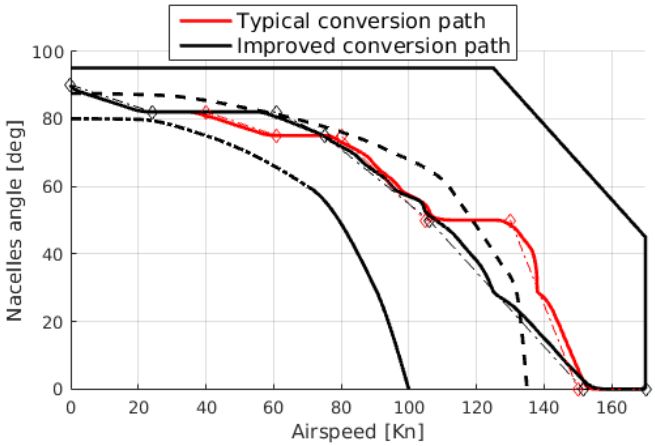

Figure 6.31: Improved conversion path

The commands history presents oscillations similar to that present in the typical conversion manoeuvre as can be seen in figure 6.32. The command derivatives reach a maximum value of about 1.5 in/s which is considered acceptable. As in all manoeuvre exposed, also in this improved manoeuvre the commands frequency content stays within the pilot bandwidth as shown in figure 6.33. The commands spectrum shown in this picture is very similar to that of the typical conversion manoeuvre, reported in figure 3.7. This brief commands analysis shows that the command histories of both conversions are easily replicable by a helicopter pilot.

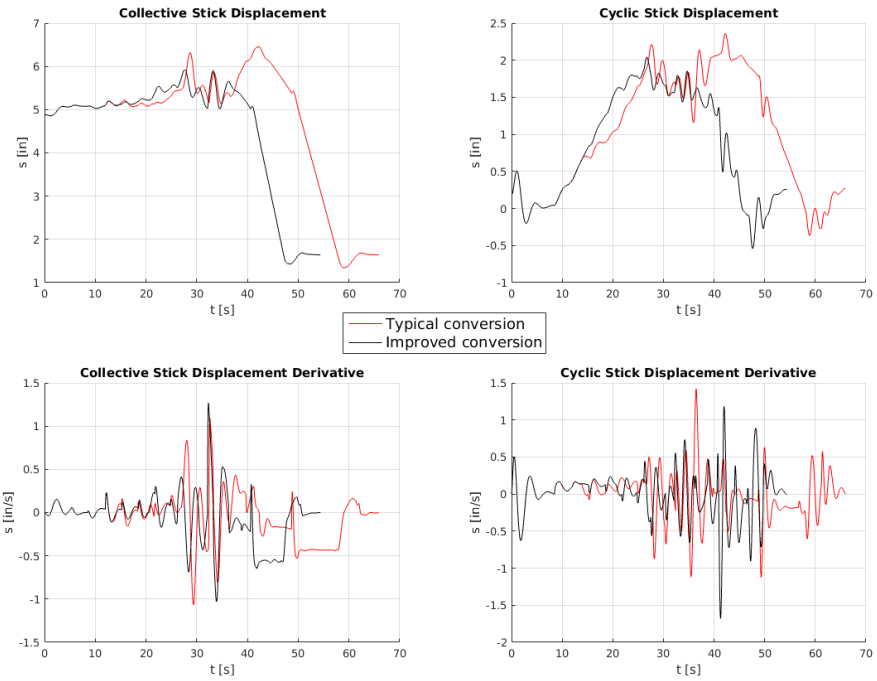

Figure 6.32: Improved conversion manoeuvre command histories

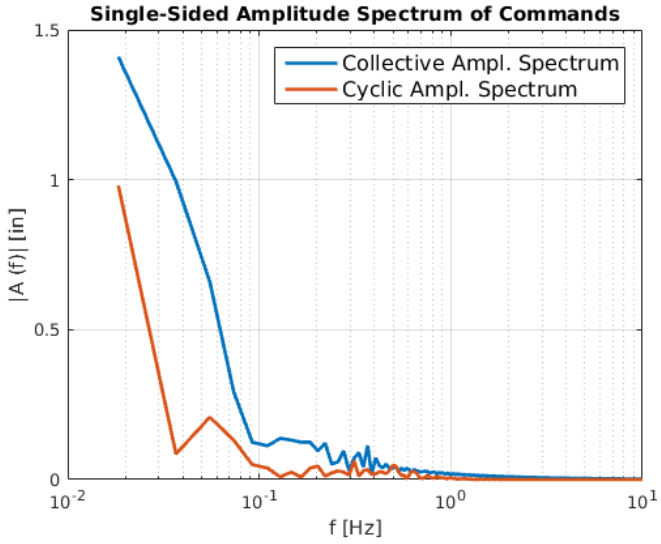

Figure 6.33: Improved conversion manoeuvre commands spectrum

The restrained nacelles rotational speed implies a moderate oscillating X_g, as shown in figure 6.34. As can be seen the conversion time is reduced by about eleven seconds, going from 59.7 to 48.6 seconds. Moreover, this equals the time required to accomplish the near stall conversion manoeuvre introduced in 6.4.1.

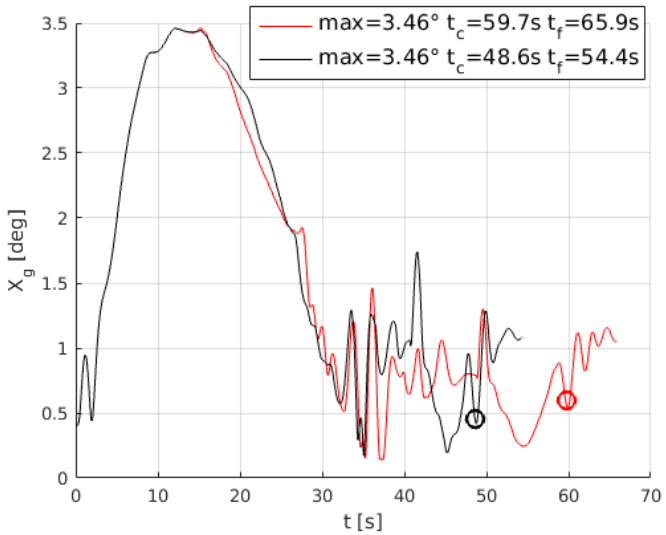

Figure 6.34: Improved conversion manoeuvre X_g trend

Then this new conversion strategy just introduced has the following advantages:

- the aircraft stays sufficiently close to the corridor center and therefore the manoeuvre safety is respected
- pilot control effort is reduced because of the lower nacelles tilting rate and the automatic nacelles control
- the aircraft acceleration profile continually increases as that reported in table 6.2, implying a reduced conversion time.

Chapter 7

Conclusions and future developments

This work has shown the effectiveness of the LPV technique in reconstructing the aircraft nonlinear dynamics starting from a database of LTI models of the tiltrotor. The virtual pilot model derived from the Modified Optimal Control pilot Model (MOCM) can effectively stabilize the aircraft and track the conversion reference imparting commands reproducible by a real helicopter pilot. Therefore the closed loop system *XV-15 LPV model − virtual pilot* fairly represents the true aircraft dynamics during a conversion manoeuvre. Optimization results in section 6.3 show that in the first conversion part it's only possible to limit the maximum X_g values to be close to X_g offset (or trim) values, assuming a low nacelles rate as 1 deg/s. It has also been shown a direct correlation between the nacelles angle rate and the high X_g values due to X_g oscillation. Therefore to contain the blades flapping it's essential to keep the nacelles rotational speed as low as possible during the whole conversion. The manoeuvre safety maximization has been discussed in section 6.4. Results show that it's possible to maximize the manoeuvre safety staying at the center of the conversion corridor but this imply a restrained aircraft acceleration, leading to more pilot effort and more time required to complete the conversion. If instead a typical acceleration profile is adopted then the last part of the conversion needs a high nacelles rotational speed leading to abrupt pilot commands and high X_g values due to oscillations. Then a compromise solution has been proposed in section 6.5. Deviating slightly the aircraft path from the corridor center is possible to achieve a conversion manoeuvre that guarantee safety, have an X_g trend similar to that of a typical conversion, reduce pilot workload in tracking the corridor reference path and also reduce the time required to complete the conversion of about eleven seconds. These manoeuvre improvements have been achieved thanks to the significant modifications introduced with respect to the standard manoeuvre.

Future developments of this work could be the in depth study of the nacelles automatic control system and its pilot interface required to perform the optimal manoeuvre proposed. Exploiting the complete XV-15 state-space models inclusive of both rotor and of antisymmetric modes it would be possible to study antisymmetric manoeuvres following the same implementation scheme used in this work to simulate the conversion manoeuvre. It is also possible to study the blades root stress including in the state-space models higher frequency rotor modes. Also, simulation results should be validated through a non-linear model of the aircraft, operation that cannot be performed using the CAMRAD/JA software with which state-space models have been created.

Appendix A

State-Space models

Some state-space models of the XV-15 models database are reported below. Models inputs are u_{COLL} and u_{CYCL}. The states list is reported in table 2.1.

State-space model at $V = 0$ Kn, $\psi = 90°$:

```
A =

   1.0e+04 *

  Columns 1 through 12

         0         0         0         0         0         0    0.0001         0         0         0         0         0
         0         0         0         0         0         0         0    0.0001         0         0         0         0
         0         0         0         0         0         0         0         0    0.0001         0         0         0
         0         0         0         0         0         0         0         0         0    0.0001         0         0
         0         0         0         0         0         0         0         0         0         0    0.0001         0
         0         0         0         0         0         0         0         0         0         0         0    0.0001
   -4.2360   -0.0002    0.0021    0.0009    0.0010    0.0000   -0.0031   -0.0000    0.0000    0.0000   -0.0000    0.0000
    0.0053   -3.1607   -0.2086    0.7912   -0.1984    0.0000   -0.0000   -0.0033   -0.0126   -0.0032   -0.0000    0.0032
    0.0026    0.2084   -3.1599    0.1977    0.7914    0.0012    0.0000    0.0126   -0.0033    0.0000   -0.0032    0.0004
    0.0002    0.1641   -0.0031   -0.0041   -0.2116    0.0000   -0.0000   -0.0001    0.0000   -0.0034   -0.0126    0.0031
   -0.0024    0.0031    0.1642    0.2116   -0.0040    0.0000    0.0000    0.0000   -0.0001    0.0126   -0.0034   -0.0132
    0.0001   -0.0000    0.0003   -0.0004    0.0001   -0.0000    0.0000    0.0000   -0.0000    0.0000   -0.0000   -0.0000
    0.0002    0.0004   -0.0022    0.0011   -0.0004   -0.0032         0         0         0   -0.0000    0.0000    0.0000
   -0.0381   -0.0001   -0.0000   -0.0000   -0.0000   -0.0000         0         0         0    0.0000    0.0000    0.0000
         0         0         0         0         0    0.0000         0         0         0         0         0         0

  Columns 13 through 15

         0         0         0
         0         0         0
         0         0         0
         0         0         0
         0         0         0
         0         0         0
    0.0000   -0.0013         0
   -0.0000   -0.0000         0
   -0.0001    0.0000         0
    0.0000    0.0000         0
    0.0001    0.0000         0
    0.0000    0.0000         0
   -0.0000    0.0000         0
   -0.0000   -0.0001         0
    0.0000   -0.0001   -0.0000


B =

   1.0e+03 *

         0         0
         0         0
         0         0
         0         0
         0         0
         0         0
    1.0625   -0.0000
   -0.0000   -0.0000
   -0.0000   -1.3011
   -0.0000   -0.0000
   -0.0000   -0.0199
   -0.0000   -0.0000
         0         0
         0         0
         0         0
```

State-space model at $V = 50$ Kn, $\psi = 90°$:

```
A =

   1.0e+04 *

  Columns 1 through 12

         0         0         0         0         0         0    0.0001         0         0         0         0         0
         0         0         0         0         0         0         0    0.0001         0         0         0         0
         0         0         0         0         0         0         0         0    0.0001         0         0         0
         0         0         0         0         0         0         0         0         0    0.0001         0         0
         0         0         0         0         0         0         0         0         0         0    0.0001         0
         0         0         0         0         0         0         0         0         0         0         0    0.0001
   -4.2355    0.0068   -0.1309   -0.0298    0.0028   -0.0002   -0.0030    0.0000   -0.0002    0.0003    0.0013   -0.0001
    0.0224   -3.1414   -0.1968    0.7984   -0.2148    0.0000    0.0000   -0.0032   -0.0126   -0.0036   -0.0001    0.0035
    0.0048    0.1994   -3.1732    0.1929    0.7929    0.0013   -0.0004    0.0126   -0.0031   -0.0001   -0.0031    0.0003
    0.0068    0.1684   -0.0027   -0.0052   -0.2152    0.0000    0.0000   -0.0000    0.0000   -0.0034   -0.0126    0.0031
    0.0635    0.0029    0.1712    0.2143   -0.0042    0.0000   -0.0000    0.0000   -0.0000    0.0126   -0.0034   -0.0132
    0.0001   -0.0000    0.0002   -0.0004    0.0000    0.0000    0.0000   -0.0000    0.0000    0.0000   -0.0000   -0.0000
    0.0001    0.0003   -0.0020    0.0011   -0.0003   -0.0032         0         0         0   -0.0000    0.0000    0.0007
   -0.0398   -0.0007   -0.0055   -0.0002    0.0004    0.0003         0         0         0    0.0000    0.0000    0.0083
         0         0         0         0         0    0.0084         0         0         0         0         0         0

  Columns 13 through 15

         0         0         0
         0         0         0
         0         0         0
         0         0         0
         0         0         0
         0         0         0
   -0.0000   -0.0012         0
   -0.0000    0.0001         0
   -0.0001   -0.0002         0
    0.0000    0.0000         0
    0.0001    0.0000         0
   -0.0000   -0.0000         0
   -0.0000    0.0000         0
   -0.0000   -0.0001         0
   -0.0000   -0.0001   -0.0000


B =

   1.0e+03 *

         0         0
         0         0
         0         0
         0         0
         0         0
         0         0
    1.0625    0.0001
   -0.0000   -0.0000
   -0.0000   -1.2959
   -0.0000   -0.0001
   -0.0000   -0.0192
   -0.0000   -0.0001
         0   -0.0000
         0   -0.0002
         0         0
```

State-space model at $V = 90$ Kn, $\psi = 75°$:

```
A =

   1.0e+04 *

  Columns 1 through 12

         0         0         0         0         0         0    0.0001         0         0         0         0         0
         0         0         0         0         0         0         0    0.0001         0         0         0         0
         0         0         0         0         0         0         0         0    0.0001         0         0         0
         0         0         0         0         0         0         0         0         0    0.0001         0         0
         0         0         0         0         0         0         0         0         0         0    0.0001         0
         0         0         0         0         0         0         0         0         0         0         0    0.0001
   -4.2699    0.0234   -0.2280   -0.0516   -0.0042   -0.0005   -0.0031   -0.0000   -0.0005    0.0004    0.0021   -0.0008
    0.0423   -3.1297   -0.1783    0.8118   -0.1760    0.0000   -0.0000   -0.0033   -0.0126   -0.0029   -0.0005    0.0030
   -0.0414    0.2293   -3.2783    0.0395    0.7564    0.0016   -0.0010    0.0126   -0.0032   -0.0004   -0.0007    0.0008
    0.0121    0.1827    0.0019   -0.0028   -0.2232    0.0000   -0.0000   -0.0000    0.0000   -0.0035   -0.0126    0.0031
    0.1093    0.0072    0.1803    0.2071   -0.0094    0.0000   -0.0000    0.0000   -0.0000    0.0125   -0.0034   -0.0130
   -0.0003    0.0000    0.0002   -0.0003    0.0000   -0.0000    0.0000    0.0000    0.0000   -0.0000   -0.0000   -0.0001
    0.0115    0.0001    0.0007    0.0001   -0.0001   -0.0032         0         0         0   -0.0000   -0.0000    0.0006
   -0.0414   -0.0009   -0.0109   -0.0003    0.0006    0.0001         0         0         0    0.0000    0.0001    0.0149
         0         0         0         0         0    0.0152         0         0         0         0         0         0

  Columns 13 through 15

         0         0         0
         0         0         0
         0         0         0
         0         0         0
         0         0         0
         0         0         0
    0.0003   -0.0012         0
   -0.0000    0.0000         0
   -0.0001   -0.0001         0
    0.0000    0.0000         0
    0.0001    0.0001         0
    0.0000   -0.0000         0
   -0.0000    0.0000         0
    0.0000   -0.0001         0
   -0.0000   -0.0001   -0.0000


B =

   1.0e+03 *

         0         0
         0         0
         0         0
         0         0
         0         0
         0         0
    1.3818    0.0004
   -0.0000   -0.0000
   -0.0000   -1.2434
   -0.0000   -0.0003
   -0.0000   -0.0169
   -0.0000   -0.0003
         0   -0.0001
         0   -0.0007
         0         0
```

State-space model at $V = 120$ Kn, $\psi = 60°$:

```
A =

   1.0e+04 *

  Columns 1 through 12

         0         0         0         0         0         0    0.0001         0         0         0         0         0
         0         0         0         0         0         0         0    0.0001         0         0         0         0
         0         0         0         0         0         0         0         0    0.0001         0         0         0
         0         0         0         0         0         0         0         0         0    0.0001         0         0
         0         0         0         0         0         0         0         0         0         0    0.0001         0
         0         0         0         0         0         0         0         0         0         0         0    0.0001
   -4.3009    0.0308   -0.2966   -0.0761   -0.0083   -0.0009   -0.0032   -0.0000   -0.0006    0.0005    0.0028   -0.0013
    0.0394   -3.1230   -0.1846    0.7960   -0.1026    0.0000   -0.0000   -0.0034   -0.0126   -0.0016   -0.0005    0.0017
   -0.0896    0.2326   -3.3107   -0.0865    0.7406    0.0016   -0.0012    0.0126   -0.0033   -0.0004    0.0012    0.0010
    0.0125    0.2016    0.0030   -0.0034   -0.2296   -0.0000   -0.0000   -0.0000    0.0000   -0.0035   -0.0127    0.0031
    0.1456    0.0080    0.2037    0.2072   -0.0109    0.0000   -0.0000    0.0000   -0.0000    0.0125   -0.0034   -0.0131
   -0.0007    0.0000    0.0002   -0.0000   -0.0000   -0.0000    0.0000    0.0000    0.0000   -0.0000   -0.0000   -0.0002
    0.0234    0.0003    0.0043   -0.0009   -0.0002   -0.0032         0         0         0   -0.0000   -0.0000    0.0008
   -0.0419   -0.0010   -0.0155   -0.0026    0.0006    0.0001         0         0         0    0.0000    0.0001    0.0199
         0         0         0         0         0    0.0202         0         0         0         0         0         0

  Columns 13 through 15

         0         0         0
         0         0         0
         0         0         0
         0         0         0
         0         0         0
         0         0         0
    0.0006   -0.0011         0
   -0.0000    0.0000         0
   -0.0001   -0.0001         0
    0.0000    0.0000         0
    0.0000    0.0002         0
    0.0000   -0.0000         0
   -0.0000    0.0000         0
    0.0000   -0.0001         0
   -0.0000   -0.0001   -0.0000


B =

   1.0e+03 *

         0         0
         0         0
         0         0
         0         0
         0         0
         0         0
    1.6224    0.0007
   -0.0000   -0.0000
   -0.0000   -1.0970
   -0.0000   -0.0005
   -0.0000   -0.0137
   -0.0000   -0.0005
         0   -0.0001
         0   -0.0012
         0         0
```

State-space model at $V = 150$ Kn, $\psi = 30°$:

```
A =

   1.0e+04 *

  Columns 1 through 12

         0         0         0         0         0         0    0.0001         0         0         0         0         0
         0         0         0         0         0         0         0    0.0001         0         0         0         0
         0         0         0         0         0         0         0         0    0.0001         0         0         0
         0         0         0         0         0         0         0         0         0    0.0001         0         0
         0         0         0         0         0         0         0         0         0         0    0.0001         0
         0         0         0         0         0         0         0         0         0         0         0    0.0001
   -4.2943    0.0216   -0.1773   -0.0127   -0.0071   -0.0013   -0.0035   -0.0000   -0.0004    0.0003    0.0014   -0.0024
    0.0265   -3.1660   -0.2081    0.7833    0.0297    0.0000   -0.0000   -0.0036   -0.0126    0.0006   -0.0003   -0.0006
    0.0436    0.2450   -3.2048   -0.1002    0.7434    0.0009   -0.0009    0.0126   -0.0036   -0.0003    0.0014    0.0020
    0.0085    0.2263    0.0012   -0.0056   -0.2233   -0.0000   -0.0000   -0.0000   -0.0000   -0.0035   -0.0126    0.0032
    0.1258    0.0057    0.2333    0.2155   -0.0095    0.0000   -0.0000   -0.0000   -0.0000    0.0126   -0.0035   -0.0133
   -0.0014   -0.0000    0.0007    0.0004    0.0000   -0.0000    0.0000    0.0000    0.0000    0.0000   -0.0000   -0.0002
    0.0441    0.0006    0.0066   -0.0010   -0.0003   -0.0032         0         0         0   -0.0000   -0.0000    0.0011
   -0.0297   -0.0004   -0.0158   -0.0073    0.0002    0.0001         0         0         0    0.0000    0.0002    0.0249
         0         0         0         0         0    0.0253         0         0         0         0         0         0

  Columns 13 through 15

         0         0         0
         0         0         0
         0         0         0
         0         0         0
         0         0         0
         0         0         0
    0.0012   -0.0007         0
   -0.0000    0.0000         0
   -0.0003   -0.0001         0
   -0.0000    0.0000         0
   -0.0000    0.0002         0
    0.0000   -0.0000         0
   -0.0001    0.0000         0
    0.0000   -0.0001         0
   -0.0000   -0.0001   -0.0000


B =

   1.0e+03 *

         0         0
         0         0
         0         0
         0         0
         0         0
         0         0
    2.8753    0.0010
   -0.0000   -0.0000
   -0.0000   -0.6259
   -0.0000   -0.0008
   -0.0000   -0.0071
   -0.0000   -0.0008
         0   -0.0002
         0   -0.0018
         0         0
```

State-space model at $V = 180$ Kn, $\psi = 0°$:

```
A =

   1.0e+04 *

  Columns 1 through 12

         0         0         0         0         0         0    0.0001         0         0         0         0         0
         0         0         0         0         0         0         0    0.0001         0         0         0         0
         0         0         0         0         0         0         0         0    0.0001         0         0         0
         0         0         0         0         0         0         0         0         0    0.0001         0         0
         0         0         0         0         0         0         0         0         0         0    0.0001         0
         0         0         0         0         0         0         0         0         0         0         0    0.0001
   -4.4312   -0.0140   -0.0071    0.0066    0.0074   -0.0013   -0.0038   -0.0000   -0.0000    0.0001    0.0001   -0.0033
   -0.0182   -3.3379   -0.2486    0.7688    0.1623    0.0000   -0.0000   -0.0040   -0.0126    0.0025   -0.0000   -0.0027
    0.0234    0.2503   -3.3277   -0.1563    0.7682    0.0001   -0.0001    0.0126   -0.0040   -0.0000    0.0024    0.0027
    0.0017    0.2448   -0.0019   -0.0077   -0.2138    0.0000   -0.0000   -0.0000   -0.0000   -0.0034   -0.0126    0.0032
    0.0118    0.0024    0.2452    0.2139   -0.0079    0.0000   -0.0000   -0.0000   -0.0000    0.0126   -0.0034   -0.0135
   -0.0025   -0.0000    0.0013    0.0007    0.0000    0.0000   -0.0000   -0.0000   -0.0000    0.0000   -0.0000   -0.0002
    0.0555    0.0003    0.0014    0.0006   -0.0000   -0.0032         0         0         0   -0.0000   -0.0000   -0.0012
    0.0003    0.0004   -0.0153   -0.0105   -0.0003   -0.0002         0         0         0   -0.0000    0.0002    0.0300
         0         0         0         0         0    0.0304         0         0         0         0         0         0

  Columns 13 through 15

         0         0         0
         0         0         0
         0         0         0
         0         0         0
         0         0         0
         0         0         0
    0.0015    0.0000         0
    0.0000    0.0000         0
    0.0000   -0.0006         0
    0.0000   -0.0000         0
   -0.0000    0.0002         0
    0.0000   -0.0000         0
   -0.0001    0.0000         0
   -0.0000   -0.0001         0
    0.0000   -0.0001   -0.0000


B =

   1.0e+03 *

         0         0
         0         0
         0         0
         0         0
         0         0
         0         0
    3.0447    0.0011
   -0.0000    0.0000
    0.0000   -0.0016
   -0.0000   -0.0011
   -0.0000   -0.0000
    0.0000   -0.0011
         0    0.0000
         0   -0.0026
         0         0
```

Appendix B

Control chain flexibility

The following table reports the Δ_f values in degrees on trim points.

V [Kn]	$\psi = 90°$	$\psi = 75°$	$\psi = 60°$	$\psi = 30°$	$\psi = 0°$
0	-3.3817				
5	-3.3785				
10	-3.3829				
20	-3.3829				
30	-3.3811	-3.3512			
40	-3.3775	-3.3212			
50	-3.3760	-3.3105			
60	-3.3991	-3.3011	-3.2261		
70	-3.4166	-3.3103	-3.2414		
80	-3.4977	-3.3513	-3.2762		
90	-3.5765	-3.4001	-3.3524	-3.4476	
100	-3.6888	-3.4744	-3.4260	-3.5305	
110	-3.8334	-3.5727	-3.5049	-3.6001	-3.6318
120		-3.6795	-3.5969	-3.6624	-3.6818
130		-3.7831	-3.6883	-3.7157	-3.7168
140		-3.9043	-3.7652	-3.7586	-3.7420
150		-4.0368	-3.8493	-3.7948	-3.7617
160			-3.9358	-3.8308	-3.7751
170				-3.8605	-3.7854
180				-3.8877	-3.7910
190					-3.7952
200					-3.8013
210					-3.8111
220					-3.8248
230					-3.8377

Appendix C

Model Trims/Offsets

In the following table from row 1 to row 15 are reported the trim values of state-space models in appendix A. The complete table contains instead the state offset values used in the LPV implementation.

$V[Kn]$	*0*	*50*	*90*	*120*	*150*	*180*
$\psi_n[deg]$	*90*	*90*	*75*	*60*	*30*	*0*
$x_r(1)$	0.1481	0.1296	0.1461	0.2264	0.3823	0.4805
$x_r(2)$	0	0	0	0	0	0
$x_r(3)$	-0.0070	-0.0368	-0.0740	-0.0780	-0.0496	-0.0262
$x_r(4)$	0.0070	0.0039	0.0214	0.0044	-0.0165	0.0204
$x_r(5)$	0.0008	-0.0612	-0.0208	-0.0030	0.0034	0.0066
$x_r(6)$	0.0080	-0.0795	-0.0388	-0.0380	-0.0380	0.0470
$x_r(7)$	0	0	0	0	0	0
$x_r(8)$	0	0	0	0	0	0
$x_r(9)$	0	0	0	0	0	0
$x_r(10)$	0	0	0	0	0	0
$x_r(11)$	0	0	0	0	0	0
$x_r(12)$	0	0	0	0	0	0
$x_r(13)$	0	84.0687	151.6890	202.2586	252.8232	303.2713
$x_r(14)$	0	-6.6990	-5.8883	-7.6816	-9.6020	14.2648
$x_r(15)$	0	0	0	0	0	0
$x_r(16)$	0	0	0	0	0	0
$x_r(17)$	0	0	0	0	0	0
$x_r(18)$	0	0	0	0	0	0
$x_r(19)$	0	0	0	0	0	0
$x_r(20)$	4.8830	4.3005	4.9267	5.9073	5.8107	1.9035
$x_r(21)$	0.1901	1.0032	2.0612	2.3611	2.0084	0.3823

Appendix D

Gain Matrixes

Some of the LQI gain matrixes are reported below.

Gain matrix at $V = 0$ Kn, $\psi = 90°$:

```
K =

  Columns 1 through 12

    1.1584   -0.0308    0.0262   -0.0805    0.3038    4.7898    0.0357    0.0001    0.0003    0.0016    0.0010    0.9550
   -0.0096    2.9250   -1.6207   21.5622  -23.6900 -251.1855   -0.0008   -0.0052   -0.0251   -0.1124   -0.1957 -111.6178

  Columns 13 through 23

   -0.2025   -3.9765    8.0091   -1.0413   14.0113    0.0176   -0.1335    9.0909   -0.0281   -6.8529    0.1384
    8.7927   -0.0612    0.2637    0.0131   -0.0983   -1.0009   13.5073   -0.0203    9.0909   -0.1665   -4.1222
```

Gain matrix at $V = 50$ Kn, $\psi = 90°$:

```
K =

  Columns 1 through 12

    1.1464   -1.0236    0.6784   -3.0845    5.6542  423.7171    0.0357    0.0024    0.0088    0.0205    0.0320   27.5594
   -0.3401    2.2424   -1.2470   15.6722  -17.2130 -290.3531   -0.0084   -0.0043   -0.0192   -0.0784   -0.1418  -77.5094

  Columns 13 through 23

   -0.4156   -3.7186    8.3073   -1.0638   13.9118    0.6192   -4.5656    9.0909   -0.8827   -7.0308   -0.0867
    8.4467    0.5519   -0.5483    0.3236   -2.9490   -0.8630   12.6569   -0.6956    9.0909    0.1089   -4.4134
```

Gain matrix at $V = 90$ Kn, $\psi = 75°$:

```
K =

  Columns 1 through 12

    1.0219   -1.1719    0.8731   -2.1990    5.6766  530.8221    0.0289    0.0030    0.0102    0.0165    0.0253   32.1834
   -0.4406    1.9230   -1.2049    7.7406  -11.0819 -728.4898   -0.0086   -0.0045   -0.0166   -0.0371   -0.0752  -79.3908

  Columns 13 through 23

    1.8509   -2.6474    6.4124   -0.9409   14.8996    0.9628   -6.7001    9.0909   -1.2619   -5.7893   -1.6883
    6.2368    3.0130   -3.9397    0.4322   -3.9327   -1.2358   14.9191   -0.9331    9.0909    2.0532   -3.5203
```

Gain matrix at $V = 120$ Kn, $\psi = 60°$:

```
K =

   1.0e+03 *

  Columns 1 through 12

    0.0009   -0.0010    0.0008   -0.0006    0.0046    0.2661    0.0000    0.0000    0.0000    0.0000    0.0000    0.0215
   -0.0004    0.0017   -0.0011   -0.0074   -0.0092   -1.0305   -0.0000   -0.0000   -0.0000   -0.0000    0.0000   -0.0767

  Columns 13 through 23

    0.0034   -0.0009    0.0029   -0.0004    0.0156    0.0009   -0.0065    0.0091   -0.0012   -0.0029   -0.0028
    0.0029    0.0037   -0.0056    0.0004   -0.0037   -0.0016    0.0174   -0.0009    0.0091    0.0033   -0.0017
```

Gain matrix at $V = 150$ Kn, $\psi = 30°$:

```
K =

  Columns 1 through 12

    0.5120   -0.2231    0.2363   -1.7282    0.9529  -79.9925    0.0143    0.0008    0.0020    0.0035    0.0151    0.0654
    0.0024    1.5676   -0.9854  -26.1062   -9.4483 -926.9264    0.0025   -0.0044   -0.0139   -0.0491    0.1926  -63.8337

  Columns 13 through 23

    1.5327    0.2774   -0.3124   -0.0753   16.9357    0.0927   -0.7662    9.0909   -0.0453    0.1274   -1.3346
   -0.3859    2.8371   -4.8573   -0.7069    1.8865   -1.7526   18.3815   -0.1336    9.0909    3.2433    0.1548
```

Gain matrix at $V = 180$ Kn, $\psi = 0°$:

```
K =

  Columns 1 through 12

    0.5215   -0.2250    0.2458   -1.7379    0.9417  -89.8369    0.0143    0.0008    0.0020    0.0033    0.0152    0.5742
    0.0067    1.5067   -0.9599  -25.1118   -9.1730 -839.6173    0.0026   -0.0043   -0.0135   -0.0492    0.1854  -57.9207

  Columns 13 through 23

    1.5354    0.2655   -0.3796   -0.0840   16.9299    0.1116   -1.0022    9.0909   -0.0545    0.1920   -1.3382
   -0.3843    2.3949   -4.1954   -0.7205    2.0001   -1.8196   18.8673   -0.1233    9.0909    2.8461    0.2041
```

Bibliography

[1] Davidson, J. B. and D. K. Schmidt. *Modified Optimal Control Pilot Model for Computer-Aided Design and Analysis*. NASA-TM-4384, National Aeronautics and Space Administration, 1992.

[2] Acree, C. W. *An Improved CAMRAD Model for Aeroelastic Stability Analysis of the XV-15 With Advanced Technology Blades*. NASA-TM-4448, National Aeronautics and Space Administration, 1993.

[3] Ferguson, S. W. *A Mathematical Model for Real Time Flight Simulation of a Generic Tilt-Rotor Aircraft*. NASA Contractor Report CR-166536, Mountain View, Calif., 1988.

[4] Ferguson, S. W. *Development and Validation of a Simulation for a Genertic Tilt-Rotor Aircraft*. NASA Contractor Report CR-166537, Mountain View, Calif., 1989.

[5] Miscellaneous from Matlab documentation. http://www.mathworks.com/.

[6] Tilt Rotor Project Office Staff. *Tilt rotor research aircraft familiarization document*. Ames Research center and U.S. Army Air Mobility R&D Laboratory, Moffett Field, Calif., 1975.

[7] Lacy, Clay. *Tiltrotor technology*. PROFESSIONAL PILOT, September 1998, p. 102.

[8] McKinney, Mike. *Flying the V-22*. Vertical Mag, 28 March 2012, `http://www.verticalmag.com/features/20112-flying-the-v-22-html/`, accessed 31 August 2016.

[9] Edwards, Paul. *609 CHECK RIDE*. PROFESSIONAL PILOT, `http://www.propilotmag.com/archives/2015/June%2015/A1_AW609_p1.html`, accessed 31 August 2016.

[10] Stephens, Ernie. *Pilot Report: Flying the AW609*. Aviation Today, 28 April 2014,
`http://www.aviationtoday.com/categories/rotocraft/Pilot-Report-Flying-the-AW609_81992.html`, accessed 31 August 2016.

[11] Johnson, Wayne. *Rotorcraft aeromechanics*. Cambridge: Cambridge University Press, 2013.

[12] Maisel, Martin D., et al. *The History of the XV-15 Tilt Rotor Research Aircraft: From Concept to Flight*. Washington, D.C.: NASA History Division, 2000.

[13] Leith, D. J. and WE. Leithead. *Survey of Gain-Scheduling Analysis & Design*. Department of Electronic & Electrical Engineering, University of Strathclyde, 50 George St., Glasgow G1 1QE.

[14] Elkind, J. I., *A survey of the Development of Models for the Human Controller*. Guidance and control II, Robert C. Langford and Charles J. Mundo, eds., Academic Press, pp. 623-343, 1964.

[15] McRuer, D., *Human Dynamics in Man-Machine Systems*. Automatica, vol. 16, no. 3, pp. 237-253, 1980.

[16] Kleinman, D. L., Baron, S. and W. H. Levison. *An optimal control model of Human Response - Part I: Theory and Validation*. Automatica, vol. 6, no. 3, pp. 357-369, 1970.

[17] Baron, S., Kleinman, D. L. and W. H. Levison. *An optimal control model of Human Response - Part II: Prediction of Human Performance in a Complex Task*. Automatica, vol. 6, no. 3, pp. 371-383, 1970.